UC Riverside

UC Riverside Electronic Theses and Dissertations

Title

Electrical Transport in Carbon Nanotubes and Graphene

Permalink

https://escholarship.org/uc/item/5d00f634

Author

Liu, Gang

Publication Date

2010

Peer reviewed|Thesis/dissertation

eScholarship.org Powered by the California Digital Library
University of California

UNIVERSITY OF CALIFORNIA
RIVERSIDE

Electrical Transport in Carbon Nanotubes and Graphene

A Dissertation submitted in partial satisfaction
of the requirements for the degree of
Doctor of Philosophy

in

Physics

by

Gang Liu

March 2010

Dissertation Committee:

Dr. Chun Ning (Jeanie) Lau Chairperson
Dr. Roland Kawakami
Dr. Shan-Wen Tsai

Copyright by
Gang Liu
2010

The Dissertation of Gang Liu is approved:

_____

_____

_____

Committee Chairperson

University of California, Riverside

Acknowledgements

I would like to express my gratitude to my thesis advisor, Professor Chun Ning (Jeanie) Lau, who supervises my five years research in her group. Jeanie has taught me not only how to do delicate physics experiment but also how to be a professional physicist. It's truly my precious experience to be one of her students.

I would like to thank my committee members, Dr. Roland Kawakami, Dr. Shan-Wen Tsai, Dr. Robert C Haddon and Dr. Ward Beyermann, and my collaborators, Dr. Jianlin Liu.

I would like to thank my wife, Yang Meng, for full support and magic luck on my research work, and for her love. And also I would like to thank my colleagues and friends, Yong Zhang, Ulas Coskun, Wenzhong Bao, Jairo Velasco Jr., Feng Miao, Hang Zhang, Lei Jing, Zeng Zhao, Hsin-Ying Chiu, Keyu Pi, Yan Li, Wei Han, Peng Wei, Hsiang-Ku Lin, Ling Yang, Deqi Wang, Tao Lin, Zuhong Xiong, Di Wu, Yong Pu, Dong Yan, Dexter Humphrey, Zheng Yang, Faxian Xiu.

In Chapter IV, two published articles, Phys. Rev. Lett., 2009 (102, 016803) and Nano Res, 2008 (2, 145), are used. In the first paper, I led the project and Yong Zhang assisted with experimental support, while in the second paper, Yong Zhang led the project and I offered assistance on side. In addition, in Chapter VI and VII, two published articles, New J. Phys., 2009 (11, 095008) and Appl. Phys. Lett., 2008 (92, 203103), are used. In the first paper, I led the project, Jairo provided the fabrication

assistance, and Wenzhong prepared the graphene flakes, while in the second paper, Jairo led the project, I provided the fabrication advice and performed measurement work, and Wenzhong prepared the graphene flakes.

ABSTRACT OF THE DISSERTATION

Electrical Transport in Carbon Nanotubes and Graphene

by

Gang Liu

Doctor of Philosophy, Graduate Program in Physics

University of California, Riverside, March 2010

This thesis summarizes our work in the past few years in the field of transport studies of carbon nanotubes and graphene. The first half of the thesis focuses on carbon nanotube (CNT) Josephson junctions (JJ) formed by coupling CNTs to superconducting electrodes. They exhibited Fabry Perot resonance patterns, enhanced differential conductance peaks, multiple Andreev reflection peaks, gate-tunable supercurrent transistor behaviors, hysteretic current-voltage line shape and "superconductor-insulator" transition. The junction behavior can be understood based on the dissipation dynamics and phase diffusion on the model of resistively and capacitively shunted junctions (RCSJ). In addition, we investigated Fano resonance on a particular device. The transport spectroscopy exhibited "inverse" Coulomb blockade structures superimposed on Fabry-Perot resonance patterns, indicating quantum interference between a channel that is well-coupled to the electrodes and

another channel that is poorly-coupled channel. Our transport data was reproduced reasonably by the simulation.

The second half of the thesis discusses our results on graphene. Firstly, by developing a technique to fabricate suspended top gates, we were able to fabricate exceedingly clean, high quality graphene *pnp* junctions. In the high magnetic fields, we observed quantum hall plateaus at fractional values, which arise from edge state propagation and equilibration in regions with different filling factors, in agreement with the theoretical predictions. In zero magnetic fields, we observed Fabry-Perot conductance oscillations in the bipolar regime, demonstrating the high quality of our devices. Secondly, we explored specular Andreev reflection and have observed conductance peaks at the superconducting energy gap in normal metal – graphene – superconductor (NS) junctions. However, the intended goal of the project, observation of specular Andreev reflection, was not achieved. As significant progress has been made towards fabrication of high quality suspended devices, we expect that specular Andreev reflection could be observed in the near future.

Table of Contents

List of Figures

List of Tables

Chapter I.

Introduction

The resistance of macroscopic object is described by the Ohm's Law. However, as the size of the object is reduced to micrometer or nanometer scale, the Ohm's Law is no longer valid, due to effects such as weak or strong localization, contact barriers, or ballistic transport. These effects are often quantum mechanical in nature, and have been at the heart of condensed matter research for the past decades. Single wall carbon nanotubes and graphene offer us interesting platforms to investigate the electron transport in the nano-scale system.

CNTs are first discovered by Sumio Iijima, and have been extensively studied for the past 20 years. SWCNT is formed by rolling up a honeycomb carbon lattice single atomic sheet, which is graphene. The diameter of CNT is around a few nanometers, and the length could reach over 1 micrometer, so a CNT is the smallest isolated one dimensional conducting wire. CNTs can be easily prepared by arc discharge, laser ablation and chemical vapor deposition (CVD), and the last method is the most popular method for research demand. A CNT has high conductivity, ultra high thermal conductivity and Young's Modulus. Interestingly, a CNT can be either metallic or semiconducting, depending on its structure, which is discussed in the Chapter II. In addition, the applications of CNT are very broad, for instance, as transistors, sensors, solar cells, fuel cells *etc*.

In particular, we are interested in the investigation of SWCNT based Josephson Junctions (Liu *et al*., 2009, Zhang *et al*., 2008) and quantum dot behaviors, which will be described in Chapter IV. We have also observed Fano resonance in a particular CNT device, which is reported in chapter V.

Graphene was first isolated from bulk graphite by Andre Geim's group in 2004 (Novoselov *et al*., 2004), and became a rising star in both the research and technology community. It can be easily obtained by mechanical exfoliation method (scotch tape method), and can be seen through a simple optical microscope. Recently graphene can be synthesized via large-scale growth on the various substrates like SiC and copper, implying that mass production of graphene for industrial applications is close to the reality. This one-atomic thick two dimensional sheet exhibits exceptional electronic properties (Novoselov *et al*., 2005, Zhang *et al*., 2005), including bipolar electric field effect, linear energy dispersion relation at low energy, anomalous quantum Hall effects *etc*. With electrical field effect, graphene can be doped by the electrons or holes, and the conductivity of graphene is finite at half filling (Dirac Point). Because graphene's energy dispersion is linear, the quasiparticles in the graphene are called massless fermions resembling neutrinos. One of the most striking consequence of graphene is that its Hall conductance is quantized at unusual values of $4(N+\frac{1}{2})(e^2/h)$, where the factor of 4 is due to double valley and double spin degeneracy, N is Landau level index, e is electron charge and h is Plant's constant. In addition, band gap engineering based on graphene nanoribbon and bilayer graphene

implies that graphene may potentially replace silicon in the semiconductor industry.

In this thesis we focus in particular on graphene *pnp* junctions system, which exhibits novel phenomena such as Klein tunneling (Katsnelson *et al*., 2006), Veselago lensing (Cheianov *et al*., 2007) and quantum Hall Effect with fractional values of conductance (Williams *et al*., 2007, Ozyilmaz *et al*., 2007) (though not to be confused with fractional quantum Hall effect). We invented a multiple lithography technique to fabricate suspended local gate for graphene *pnp* junctions (Liu *et al*., 2008) (chapter VI), and quantum Hall effect at fractional values and Fabry-Perot oscillations are observed in the high quality devices (Velasco *et al*., 2009) (chapter VII). We have also investigated graphene NS junctions (chapter VIII), with the goal of observing specular Andreev reflection at the NS interface. Finally, I will conclude the thesis with a brief conclusion and outlook for future work.

Reference

Cheianov, V. V., *et al*., Science 2007, 315, 1252.

Katsnelson, M. I, *et al*., Nature Phys 2006, 2, 620–625.

Liu, G., *et al*., Phys. Rev. Lett., 2009, 102, 016803.

Liu, G., *et al*., Appl. Phys. Lett., 2008, 92, 203103.

Novoselov, K. S. *et al*., Science, 2004, 306, 666–669.

Novoselov, K. S., *et al*., Nature, 2005, 438, 197–200.

Ozyilmaz, B., *et al*., Phys. Rev. Lett. 2007, 99, 166804.

Velasco Jr., J., *et al*., New J. Phys., 2009, 11, 095008.

Williams, J. R., *et al*., Science 2007, 317, 638.

Zhang, Y., *et al*., Nature, 2005, 438, 201–204.

Zhang, Y., *et al*., *Nano Res*, 2008, 2, 145.

Chapter II.

Introduction to Carbon Nanotubes and Graphene

Single wall Carbon nanotubes and graphene are the most popular Carbon material in the condensed matter research. Based on energy dispersion relation, SWCNT are divided into two types, metallic and semiconducting, while graphene is a semi-metal or zero-gap semiconductor. In general, graphene is structurally identical to rolled up graphene, thus we will start from atomic structure and electron band structure of graphene.

II-1. the Structure of Graphene

Graphene is a single layer of graphite, a 2D single carbon sheet with hexagonal lattice. The atomic structure in real space is shown in Fig. II-1a.

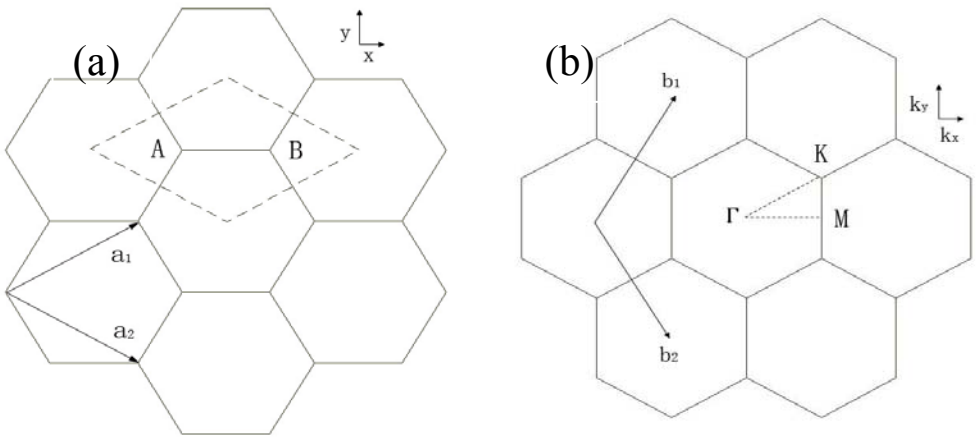

Fig. II-1. graphene hexagonal lattice, (a) real space lattice of graphene. vector a_1 and

a_2 are primitive vectors, the dotted rhombus is the unit cell, (b) reciprocal lattice of graphene, vector b_1 and b_2 are reciprocal vectors, K, M and Γ are high symmetry points.

In the real space, the distance between two carbon atoms is 0.142nm. The unit cell of hexagonal lattice is a rhombus as indicated in Fig. II-1a, instead of a hexagon. Each unit cell has two carbon atoms A and B. The primitive vector of unit cell is $\overrightarrow{a_1}$ and $\overrightarrow{a_2}$ expressed as

$$\overrightarrow{a_1} = (\frac{\sqrt{3}}{2}a, \frac{1}{2}a) \qquad \overrightarrow{a_2} = (\frac{\sqrt{3}}{2}a, -\frac{1}{2}a)$$

where $a = |\overrightarrow{a_1}| = |\overrightarrow{a_2}| = \sqrt{3}a = 0.246nm$.

In the reciprocal space, the unit vectors $\overrightarrow{b_1}$ and $\overrightarrow{b_2}$ are expressed as

$$\overrightarrow{b_1} = (\frac{2\pi}{\sqrt{3}a}, \frac{2}{a}) \qquad \overrightarrow{b_2} = (\frac{2\pi}{\sqrt{3}a}, -\frac{2}{a})$$

Where $|\overrightarrow{b_1}| = |\overrightarrow{b_2}| = \frac{4\pi}{\sqrt{3}a}$. The directions of reciprocal unit vectors $\overrightarrow{b_1}$ and $\overrightarrow{b_2}$ are rotated by 90 degree from the real space unit vectors $\overrightarrow{a_1}$ and $\overrightarrow{a_2}$ as shown in Fig. II-1b. The lattice in the reciprocal space is still hexagonal, but the size of lattice becomes $\frac{4\pi}{3a}$. The first Brillouin zone is selected as a basic hexagon, which has three high symmetric point K (the corner of hexagon), M (the edge center) and Γ (center). In the following section, the energy dispersion relation is derived with respect to these three points.

II-2. the Energy Dispersion Relation of Graphene by Tight Bonding Method

Each carbon atom has three σ bond in sp^2 configuration, while the other sp_z orbital makes π covalent bonds. Because the π energy bands play the most important role for determining the solid state properties of graphene, we only consider π energy bands for graphene.

In the tight bonding method, we need to determine transfer integral and overlap integral matrices, which are respectively defined by

$$H_{jj'}(\vec{k}) = \left\langle \Phi_j \middle| H \middle| \Phi_{j'} \right\rangle, \qquad S_{jj'}(\vec{k}) = \left\langle \Phi_j \middle| \Phi_{j'} \right\rangle \qquad (j, j' = 1, \ldots, n)$$

where $\Phi_j(\vec{k}, \vec{r})$ is Bloch function given by

$$\Phi_j(\vec{k}, \vec{r}) = \frac{1}{\sqrt{N}} \sum_{\vec{R}}^{N} e^{i\vec{k}\cdot\vec{R}} \varphi_j(\vec{r} - \vec{R}), \qquad (j = 1, \ldots, n)$$

Here $\vec{R}$ is the position of the atom and φ_j denotes the atomic wave function in state *j*. Finally, solving the secular equation $\det[H - ES] = 0$ yields the eigenvalues of $E_i(\vec{k})$ (the energy dispersion relations).

Since graphene lattice has two inequivalent carbon atoms at A and B in Fig. II-1a, two Bloch functions provide the basis functions and the matrixes are 2*2. When we only consider nearest neighbor interaction, then,

$$\begin{aligned} H_{AA}(\vec{r}) &= \frac{1}{N} \sum_{\vec{R},\vec{R}'} e^{i\vec{k}(\vec{R}-\vec{R}')} \left\langle \varphi_A(\vec{r} - \vec{R}') \middle| H \middle| \varphi_A(\vec{r} - \vec{R}) \right\rangle \\ &= \frac{1}{N} \sum_{\vec{R}=\vec{R}'} \varepsilon_{2p} = \varepsilon_{2p} = H_{BB} \end{aligned}$$

ε_{2p} comes from $R = R'$, which is the maximum contribution to H_{AA}. (all higher order contribution will be neglected). Similarly, H_{BB} has the same expression. As for H_{AB}, three nearest neighbors B atoms relative to an A atom, need to be considered. Three vectors $\vec{R_1}$, $\vec{R_2}$ and $\vec{R_3}$ are denoted by $(\frac{a}{\sqrt{3}}, 0)$, $(-\frac{a}{2\sqrt{3}}, \frac{a}{2})$ and $(-\frac{a}{2\sqrt{3}}, -\frac{a}{2})$.

$$H_{AB}(\vec{r}) = \frac{1}{N}\sum_{\vec{R},\vec{R}'} e^{i\vec{k}(\vec{R}-\vec{R}')} \left\langle \varphi_A(\vec{r}-\vec{R}') \middle| H \middle| \varphi_B(\vec{r}-\vec{R}) \right\rangle$$

$$= \frac{1}{N}\sum_{\vec{R}} \begin{array}{l} e^{i\vec{k}(\vec{R}-\vec{R_1})} \left\langle \varphi_A(\vec{r}-\vec{R_1}) \middle| H \middle| \varphi_B(\vec{r}-\vec{R}) \right\rangle + \\ e^{i\vec{k}(\vec{R}-\vec{R_2})} \left\langle \varphi_A(\vec{r}-\vec{R_2}) \middle| H \middle| \varphi_B(\vec{r}-\vec{R}) \right\rangle + \\ e^{i\vec{k}(\vec{R}-\vec{R_3})} \left\langle \varphi_A(\vec{r}-\vec{R_3}) \middle| H \middle| \varphi_B(\vec{r}-\vec{R}) \right\rangle \end{array}$$

$$= t\left(e^{i\vec{k}\cdot\vec{R_1}} + e^{i\vec{k}\cdot\vec{R_2}} + e^{i\vec{k}\cdot\vec{R_3}}\right)$$

$$= t\left(e^{ik_x a/\sqrt{3}} + 2e^{-ik_x a/2\sqrt{3}}\cos(\frac{k_y a}{2})\right) = t\cdot f(k)$$

where $t = \left\langle \varphi_A(\vec{r}-\vec{R_j}) \middle| H \middle| \varphi_B(\vec{r}-\vec{R}) \right\rangle$. Since the Hamiltonian is a Hermitian matrix, we obtain $H_{BA} = H_{AB}^* = tf(k)^*$. Then we can obtain overlap matrix easily, $S_{AA}=S_{BB}=1$, and $S_{AB}=sf(k)=S_{BA}^*$, where $s = \left\langle \varphi_A(\vec{r}-\vec{R_j}) \middle| \varphi_B(\vec{r}-\vec{R}) \right\rangle$. So the explicit forms for H and S are written as:

$$H = \begin{pmatrix} \varepsilon_{2p} & tf(k) \\ tf(k)^* & \varepsilon_{2p} \end{pmatrix}, \quad S = \begin{pmatrix} 1 & sf(k) \\ sf(k)^* & 1 \end{pmatrix}$$

Then we solve the secular equation $\det[H - ES] = 0$, and obtain the eigenvalues $E(\vec{k})$ as a function of $f(\vec{k})$ and $\vec{k}$:

$$E(\vec{k}) = \frac{\varepsilon_{2p} \pm t\sqrt{\left|f(\vec{k})\right|^2}}{1 \pm t\sqrt{\left|f(\vec{k})\right|^2}}, \quad f(\vec{k}) = e^{ik_x a/\sqrt{3}} + 2e^{-ik_x a/2\sqrt{3}} \cos(\frac{k_y a}{2})$$

where + and – signs give the bonding π energy band and anti-bonding π^* band.

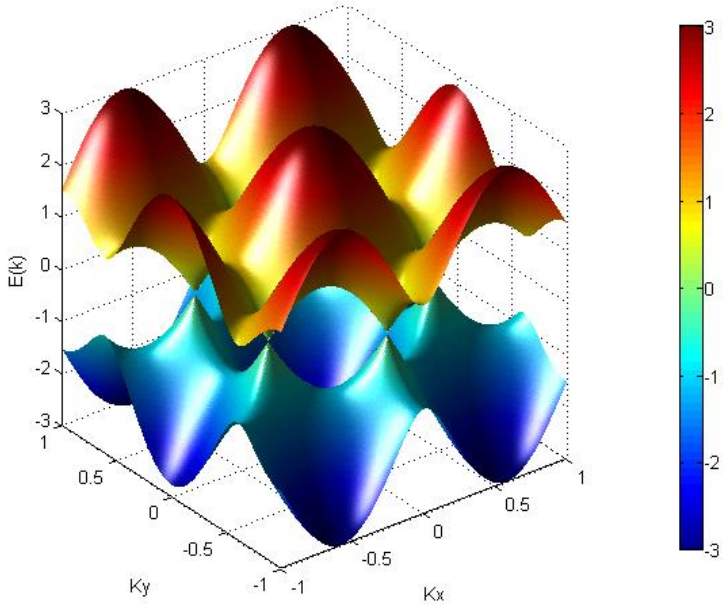

Fig. II-2. energy dispersion relations of graphene

The energy dispersion relations of graphene are plot through the Brillouin zone in Fig. II-2. We set the parameters ε_{2p}=0, t=-3.033eV and s=0.129 as the reference (Saito *et al*., 1998). The upper part of the plot is the anti-bonding π^* band, while the lower part is the π energy band. These two bands are degenerate at the K points, where the density of states is zero. So graphene is zero band gap semiconductor. At the low energy, the energy dispersion relations can be written as

$$E(\vec{k}) = \hbar v_F \left|\vec{k}\right|$$

where the Fermi velocity $v_F \sim 10^6$ m/s.

II-3. the Structure of Carbon Nanotubes

A carbon nanotube is formed by rolling up a sheet of graphene along a chiral vector $\overrightarrow{C_h}$, which is expressed as $n\overrightarrow{a_1} + m\overrightarrow{a_2}$, with a circumference of $\left|\overrightarrow{C_h}\right|$ as shown in Fig. II-1. The chiral vector determines the electronic structure of the carbon nanotube, such as metallic type, semiconducting type and the band gap. By the symmetry classification, carbon nanotubes are categorized as achiral or chiral. The achiral carbon nanotubes only include armchair and zigzag nanotube, the names of which are based on the shape of cross sectional ring. The armchair nanotubes with a chiral vector $\overrightarrow{C_h} = (n,n)$, must be metallic, while the zigzag nanotubes with a chiral vector $\overrightarrow{C_h} = (n,0)$ is only metallic if n is the integer multiple of three. The chiral nanotubes are nearly metallic with a small curvature induced band gap if n-m is the integer multiple of three, and the rest of chiral nanotubes are semiconducting.

After rolling up, point O overlaps with point A, and point B overlaps with point C. The circle of OA forms the circumference of the nanotube, and OB, which is the translational vector $\vec{T}$, is parallel to the axis of the nanotube. The diameter of a nanotube d_t is derived from the circumference of the nanotube:

$$d_t = \frac{\left|\overrightarrow{C_h}\right|}{\pi} = \frac{1}{\pi}\sqrt{\overrightarrow{C_h} \cdot \overrightarrow{C_h}} = \frac{a}{\pi}\sqrt{n^2 + m^2 + nm}$$

For example, the diameter of the nanotube with the chiral vector (4,2) is $\sqrt{28}a/\pi$, where a=2.49Å. And the energy band gap of a semiconducting nanotube is determined by its diameter, $E_g = 4\hbar v_F / 3d_t$

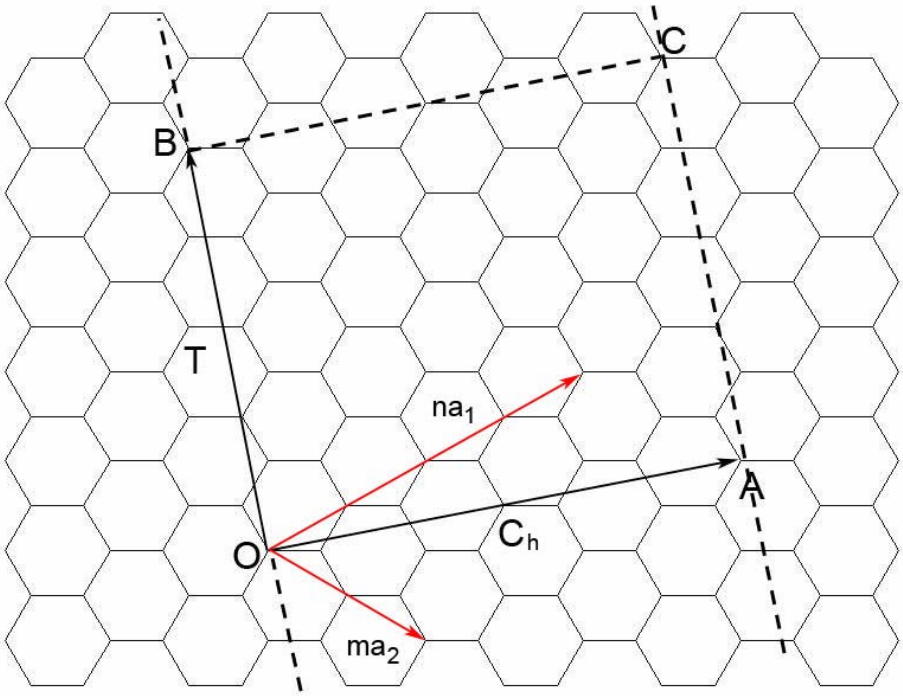

Fig. II-3. structure of a carbon nanotube is defined with the chiral vector $\overrightarrow{C_h} = \overrightarrow{OA} = (4,2)$, the translational vector $\vec{T} = \overrightarrow{OB} = (4,-5)$, and the number of hexagons N=28. The rectangle OABC denotes the unit cell of the nanotubes.

The translational vector $\vec{T}$ is defined as the unit vector of a nanotube, which is parallel to the nanotube axis and is perpendicular to the chiral vector $\overrightarrow{C_h}$. The translational vector $\vec{T}$ corresponds to the first lattice point of the graphene sheet passed by the vector $\overrightarrow{OB}$. The expression of the translational vector $\vec{T}$ is $t_1\overrightarrow{a_1} + t_2\overrightarrow{a_2}$, where

$$t_1 = \frac{2m+n}{d_R}, \qquad t_2 = -\frac{2n+m}{d_R}$$

by using $\overrightarrow{C_h} \cdot \vec{T} = 0$. And d_R is the greatest common divider of (2m+n) and (2n+m). For example, the translational vector $\vec{T}$ is (4,-5) with the chiral vector $\overrightarrow{C_h} = (4,2)$, where d_R is 2 . The magnitude of the translational vector $\vec{T}$ is $\left|\vec{T}\right| = \sqrt{3}\left|\overrightarrow{C_h}\right| / d_R$. The example $\left|\vec{T}\right|$ in Fig. II-3 is $\sqrt{21}a$. The number of the hexagons in the rectangular unit cell OABC N can be obtained by

$$N = \frac{\left|\overrightarrow{C_h} \times \vec{T}\right|}{\left|\overrightarrow{a_1} \times \overrightarrow{a_2}\right|} = \frac{2(n^2 + m^2 + nm)}{d_R}$$

meaning divide the area of nanotube unite cell by the area of the hexagon. (The number of carbon atom is the unit cell is 2N, because there are two carbon atoms in each unit cell.) In Fig. II-3, the unit cell has N=28 hexagons and 56 carbon atoms.

The reciprocal lattice vectors $\overrightarrow{K_1}$ and $\overrightarrow{K_2}$, which are in the circumferential direction and is parallel to the nanotube axis respectively, can be obtained by the relation $\overrightarrow{R_i} \cdot \overrightarrow{K_j} = \delta_{ij} 2\pi$, where $\overrightarrow{R_i}$ is the unit vector in the real space. From the relations

$$\overrightarrow{C_h} \cdot \overrightarrow{K_1} = 2\pi \qquad \vec{T} \cdot \overrightarrow{K_1} = 0$$

$$\overrightarrow{C_h} \cdot \overrightarrow{K_2} = 0 \qquad \vec{T} \cdot \overrightarrow{K_2} = 2\pi$$

The expressions of $\overrightarrow{K_1}$ and $\overrightarrow{K_2}$ are

$$\overrightarrow{K_1} = \frac{1}{N}(-t_2 \overrightarrow{b_1} + t_1 \overrightarrow{b_2}) \qquad \overrightarrow{K_2} = \frac{1}{N}(m\overrightarrow{b_1} - n\overrightarrow{b_2})$$

where $\vec{b}_1$ and $\vec{b}_2$ are the reciprocal lattice vectors of graphene. So $\vec{K}_1 = \frac{1}{28}(5\vec{b}_1 + 4\vec{b}_2)$ and $\vec{K}_2 = \frac{1}{28}(4\vec{b}_1 - 2\vec{b}_2)$ as shown in Fig. II-4 example. Since t_1 and t_2 don't have the common divider, none of $\mu\vec{K}_1$ ($\mu = 1, \cdots, N-1$) are reciprocal vectors. So the N wave vectors $\mu\vec{K}_1$ give rise to N discrete value of the k vector. The first Brillouin zone is the line segment with length of $2\pi / \left|\vec{T}\right|$ as indicated in Fig. II-4.

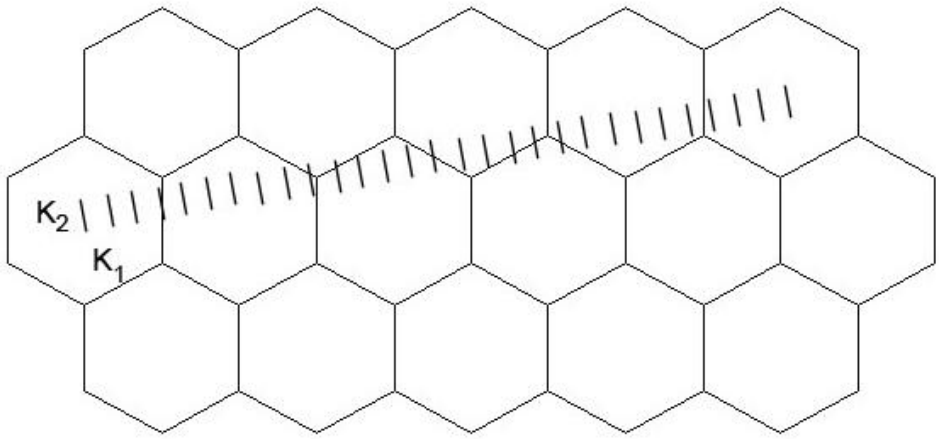

Fig. II-4. reciprocal lattice vectors $\vec{K}_1$ and $\vec{K}_2$ vectors for the example as discussed above.

The energy dispersion relation of a nanotube is

$$E(k) = E(k\frac{\vec{K}_2}{\left|\vec{K}_2\right|} + \mu\vec{K}_1), \quad (\mu = 1, \cdots, N-1, and -\frac{\pi}{T} < k < \frac{\pi}{T})$$

Since $\vec{K}_1$ has N discrete value of the wave vector, from the above relation we obtain N pair of the energy dispersion relations, which correspond to the line sections by

lines of $k\frac{\overrightarrow{K_2}}{\left|\overrightarrow{K_2}\right|}+\mu\overrightarrow{K_1}$ on the graphene 2D energy dispersion as Fig. II-2. For a nanotubes in general, if the line section cut through the K point of the graphene 2D Brillouin zone, 1D energy band of the nanotube has zero bang gap and the nanotube behaves as a metallic nanotube. Otherwise, the nanotube is semiconducting with a finite band gap between the valence band and the conduction band.

The condition of obtain metallic nanotubes is, that the ratio of the length of $\overrightarrow{YK}$ to the length of $\overrightarrow{K_1}$ is a integer, which means one of line segments cut through K point. The vector $\overrightarrow{YK}$ is expressed as

$$\overrightarrow{YK}=\frac{2n+m}{3}\overrightarrow{K_1}$$

, so the condition is that (2n+m) or (n-m) is a multiple of 3. Therefore a armchair nanotube (n, n) is always metallic, and a zigzag nanotube (n,0) is only metallic if n is a multiple of 3.

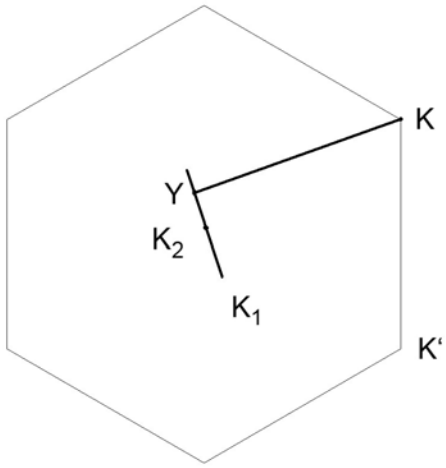

Fig. II-5. condition of obtaining a metallic nanotube: $\overrightarrow{YK}$ is the distance from K point to the first line segment $\overline{K_2}$, and is perpendicular to $\overline{K_2}$.

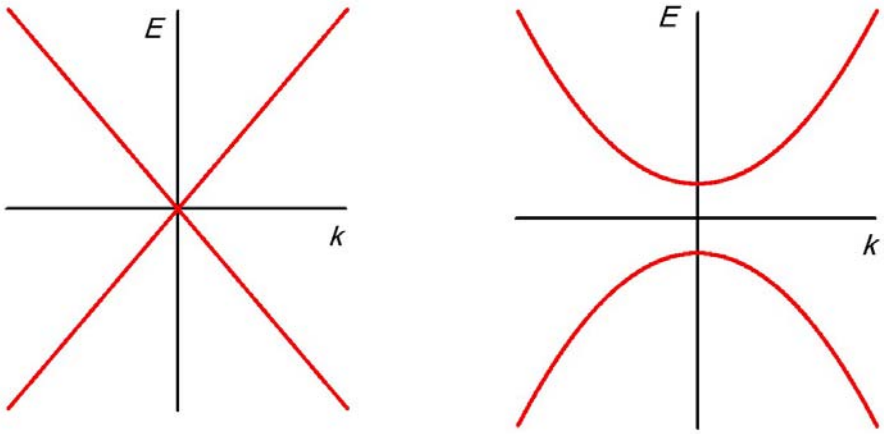

Fig. II-6. schematics of metallic (left) and semiconducting (right) CNT band structure

Reference

R. Saito, G.D., M. S. Dresselhaus, Physical Properties of Carbon Nanotubes. 1st ed. World Scientific Publishing Company, 1998.

Chapter III.

Fabrication of Carbon Nanotube Devices and Measurement Setup

III-1. Carbon Nanotube Growth with Catalyst Island Method

Single wall carbon nanotubes (SWCNT) are grown on the Si/SiO_2 wafers by standard chemical vapor deposition (CVD) method, which was first developed by Dr. Hongjie Dai's group (Kong *et al*., 1998). The recipe we are using is similar to that outlined Jarillo-Herrero *et al*., 2006.

The original catalyst solution is made of 40mg of $Fe(NO_3)_3 \cdot 9H_2O$, 2mg of $MoO_2(acac)_2$, and 30mg of Alumina nanoparticles in 30ml of de-ionized (DI) water and sonicated for ~1hr. Then the original solution is diluted by DI water for 1:5 (solution vol./ DI water vol.), the number of dilution times varies for difference experimental demand.

To pattern catalyst islands, we first use electron beam lithography (EBL) to make an array of Ti (30~40nm thick) alignment marks with 20μm spacing on clean Si/SiO_2 wafers, after performing another EBL (with PMMA/MMA as well) to open a number of 2*2μm windows among the alignment marks on prepared sample, we deposit a few nm Ti on it by sputtering coater (time 5 minutes, current:30μA). (Please see Appendix I for EBL protocol) We then deposit a drop of diluted solution on the prepared sample, and bake it on the 80^0C hot plate, wait until the solution is dry. After baking, the catalyst forms a thin film sticking to the Ti layer. Finally, the resist layers are lifted off

by placing the chips in acetone for 10 minutes, gently washing with IPA for 5 seconds and gently blowing dry with nitrogen gas.

The SWNT are grown in the high temperature furnace. The basic principle is that at the high temperature carbon atoms from methane form carbon nanotubes at catalyst particle. The growth parameters are summarized in the following table.

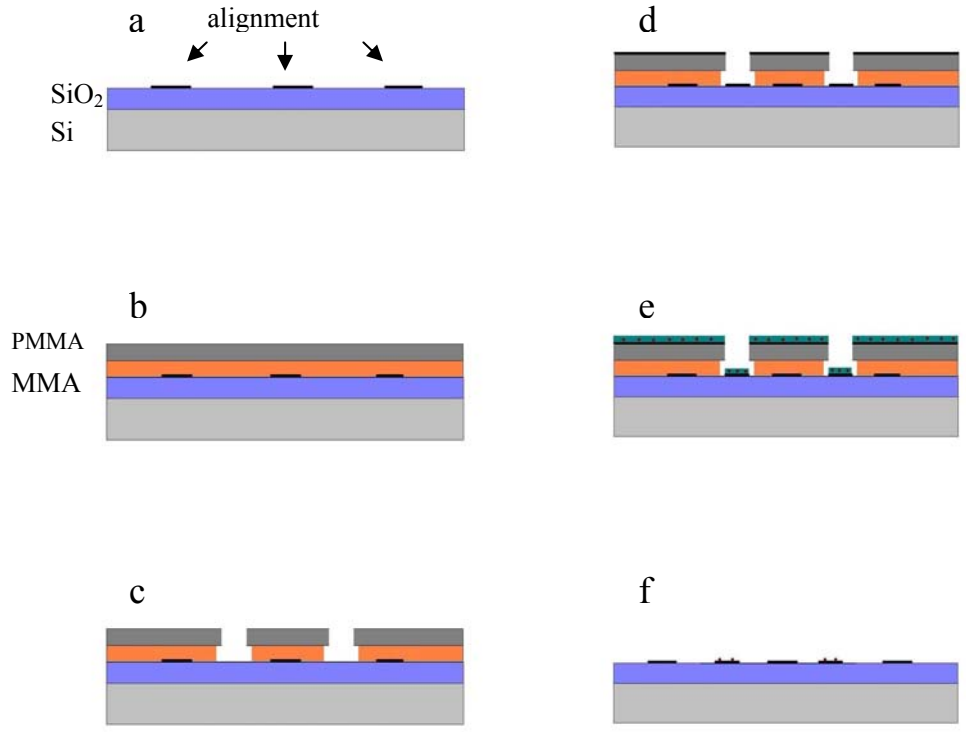

Fig. III-1. EBL for alignment marks and catalyst islands. (a), prepare alignment marks on blank wafer. (b), spin PMMA/MMA bi-layer resist on wafer. (c), open defined window by EBL. (d), deposit 5nm Ti by sputtering coater. (e), drop catalyst solution and bake at 80°C until dry, then lift-off for 10mins in Acetone. (f), the sample is ready to CNT growth

	H_2 (SLM)	Ar (SLM)	CH_4 (SLM)	
1	0	1	0	Flushing the quartz tube: 2 min
2	0.2	0.4	0	Ramp up T from 25°C to 900°C within 25 min
3	0.7	0	0.7	T=900°C, Growth time: 10 min
4	0	2	0	Heating off, Flushing:2 min
5	0	0.4	0	open oven cover @ 600°C, take sample out @300°C

Table III-1. SWNT growth recipe.

Dr. Bockrath's new recipe (Deshpande *et al*., 2008) is reported to be able to grow ultra clean SWCNT without amorphous carbon deposition. The major difference is at 3rd step: 0.5 SLM CH_4 and 0.7 SLM H_2 at 800°C within 5 min. My limited attempts with the new recipe show that it yields fewer CNT.

III-2. Device Fabrication with E-Beam Lithography and Evaporation

After CNT growth, the sample is scanned by electrical field microscope (EFM) around catalyst island area. Once a suitable length CNT is found, an image including adjacent alignment marks need to be taken. Then the following work would be design the leads and bonding pads in the NPGS software and EBL.

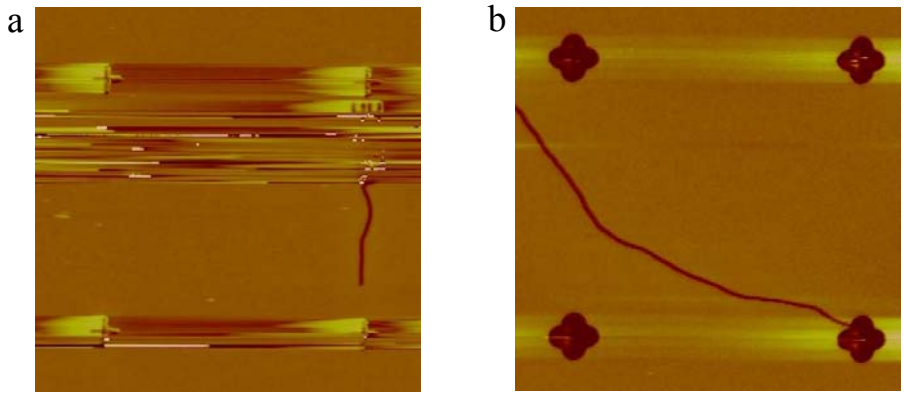

Fig. III-2. two EFM images of CNT growth from catalyst islands. (a), an example of above method. (b), a different method: catalyst islands works alignment marks as well. The spacing between alignment marks is 20μm

For the fabrication of leads and bonding pats, PMMA and LOR 3B bi-layer resist is applied. LOR can be developed separately from PMMA and leave the sample surface cleaner than MMA does. The spinning parameter for LOR is the same as MMA, but baking parameter is 190°C and 5 minutes. For the developing step, LOR need to be developed in MF319 for 6~8 seconds and rinsed by DI water for 60 seconds after developing PMMA. Then device leads (5nm Pd/ 80nm Al) are deposited by e-beam evaporation. We find that Pd is quite necessary for good contact between leads and CNT, and higher evaporation rate (4~5 A/s) is also important during the Pd deposition. At the end, the device is lift-off in PG remover at 80°C for at least 1 hour.

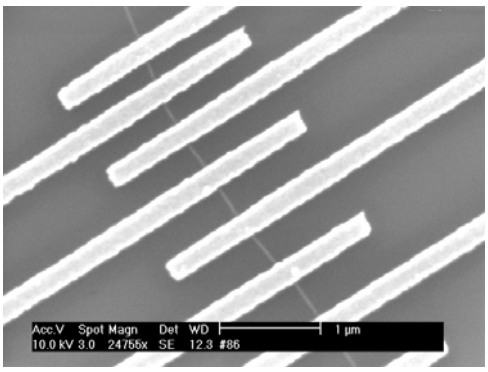

Fig. III-3. SEM image of a CNT device with different spacing leads. Leads are 5nm Pd/ 80nm Al.

III-3. Chip and Chip Carriers, Wire Bonding Parameters

The wafer is 100 mm size, highly doped Silicon(0.001~0.005 ohm-cm), 500μm thick, single side polished with 300 nm Oxide layer, ordered from University Wafer or Silicon Quest. All of fabrication and sample preparation is performed on the top of the Oxide layer, which behaves as dielectric layer between device and gate. The sandwich structure forms a standard capacitor; it allows us to control the static electric field on the device by tuning the gate voltage on the highly doped silicon layer.

For measuring devices, samples are glued to 20 pins chip carrier with small amount of silver paint. The chip carrier is the product of Spectrum Semiconductor and Materials (part number: CSB02039). The function of silver paint is to electrically connect silicon back gate to the chip carrier bottom. Then we bond wires from the chip carrier to device bonding pads with wire bonder, generally the bond on chip carrier is the first bond with 400 ultrasonic power and 30 ms time, the one on the device is the second one with 350 ultrasonic power and 30 ms time. The diagram of

each bonding pin corresponding to each foot can be found around wire bonder.

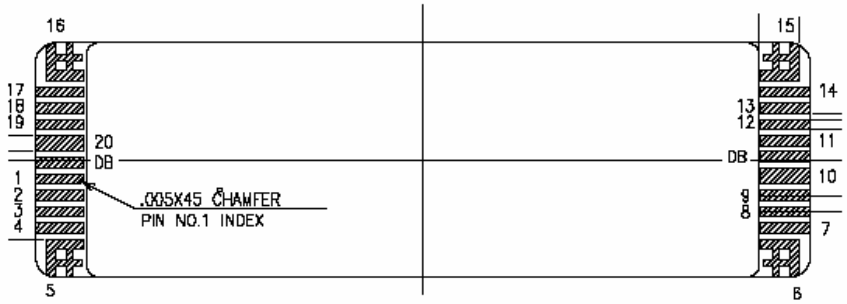

Fig. III-4. drawing of a chip carrier

III-4. He3 Refrigerator

The devices are measured in the He3 pumped cryostat produced by Oxford instrument. The base temperature of the fridge can reach 260mK, and hold for 24 hours depending on the amount of exchange gas. The chip carriers with devices are inserted onto socket on the tailpiece of insert, the tailpiece includes copper structure holder, two socket (one horizontal, the other vertical), RC filter and copper powder filter. The devices are connected through low temperature RC filer and copper powder filter to the room temperature 24 pins fisher connectors, which allow us to connect to measurement instrument.

a 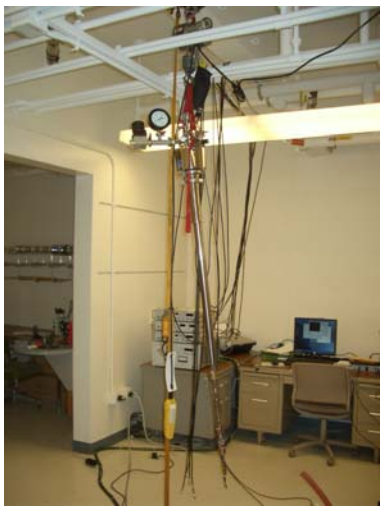 b 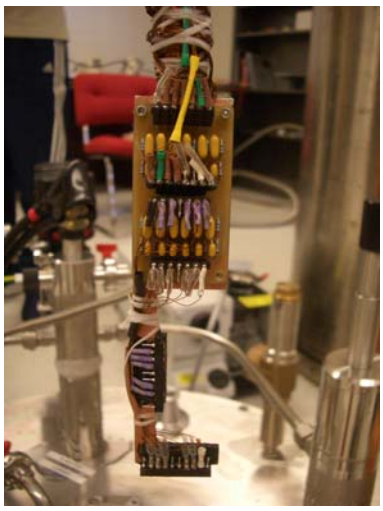

Fig. III-5. (a), photo of He3 insert. (b), photo of tail piece

Our filter system is similar to Dr Kouwenhoven's setup (Jarillo-Herrero *et al.*, 2006), and was designed and installed by Dr. Ulas Coskun. A copper powder filter and a silver paste filter are used to reduce high frequency noise (>1GHz), lowering the effective electron temperature. The two stages RC filter are used for lower frequency range, a diagram of the RC filter can be seen in the following figure. The value configuration of the RC filter is R_1=820 Ω, R_2=1.2k Ω, C_1=20nF, C_2=4.7nF. The cutoff frequency of our RC filter is about 2kHz.

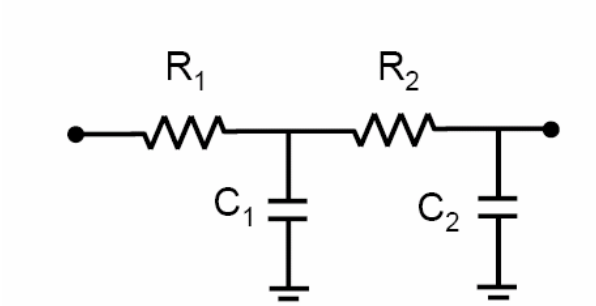

Fig. III-6. diagram of two stages RC filter.

The operation protocol of the He3 fridge can be found in Appendix II. The base temperature of cryostat can reach 260mK with the condensation of He3. First, the sample is cooled to 4K by thermal conduction of exchange helium gas after the insert is lowered into Helium bath. The exchange gas will be taken up by the charcoal sorb at low temperature. Then we pump the 1k pot, which pump liquid helium from pick-up pipe at bottom of insert. This lowers the temperature of the He3 pot and 1K pot to ~1.5K. We then set the He3 sorb temperature to 40K. The sorb is He3 sorption pump, made of activated charcoal. At high temperature (40K), the sorb releases adsorbed He3 gas, which will eventually condense in the He3 pot. After 40 minutes, all He3 gas is released from the sorb, and He3 pot is full of liquid He3, then we set the sorb temperature back to zero. At this point, the sorb starts to pump He3 vapor, thus cooling the He3 pot, and hence the sample stage that is thermally anchored to it, to ~260mK.

III-5. Measurement Circuit Setup

All the data described in the following chapters are taken in the He3 refrigerator. Typically several types of typical measurement set-ups are used, such as two probe DC voltage bias, four probe DC current bias, two probe AC voltage bias. Here we briefly describe the circuit diagram of each measurement.

The measurement interface is BNC 2090 from National instrument. Its front board has two voltage sources (DAC0out and DAC1out), eight data taking channels (ACH0~ACH7). For convenience, ACH0 is typically used for taking differential conductance or differential resistance from lock-in amplifier, ACH1 for taking converted current from current amplifier or voltage from voltage amplifier (SR560), DAC0out for voltage bias, DAC1out for gate voltage.

Two-probe DC voltage bias is the most fundamental measurement for probing device current-voltage curve. The diagram can be seen in the following figure.

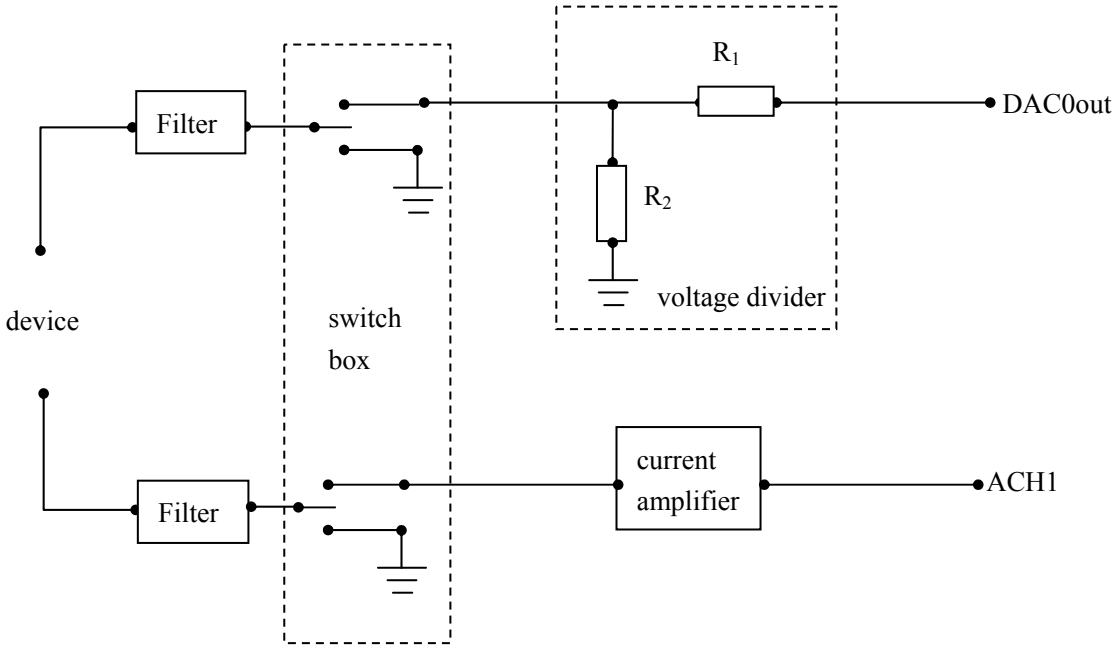

Fig. III-7. circuit diagram of DC voltage bias measurement

The DAC0out is the voltage source, and ACH1 is the channel for taking current. The voltage signal pass a voltage divider first, which divide the voltage signal by $(R_1+R_2)/R_2$. The value of R_2 is usually set much more smaller than device resistance, typically 10-100 Ω, and the value of R1 is 100 times or 1000 times larger than R_2, then $(R_1+R_2)\ /R_2 \approx R_1/R_2$. The voltage divider is crucial for reducing digital noises from the National Instrument board.. After the voltage divider, the voltage signal is applied on the device through the low temperature filters, and the current from the other end of device passes through filters and is amplified by the current amplifier. Finally the amplified signal is read by the BNC interface.

Four-probe DC current bias is usually used for eliminating the line resistance or filter resistance, and for obtaining the cleanest current-voltage characteristics of, say,

superconducting devices. The circuit diagram is illustrated in the following figure.

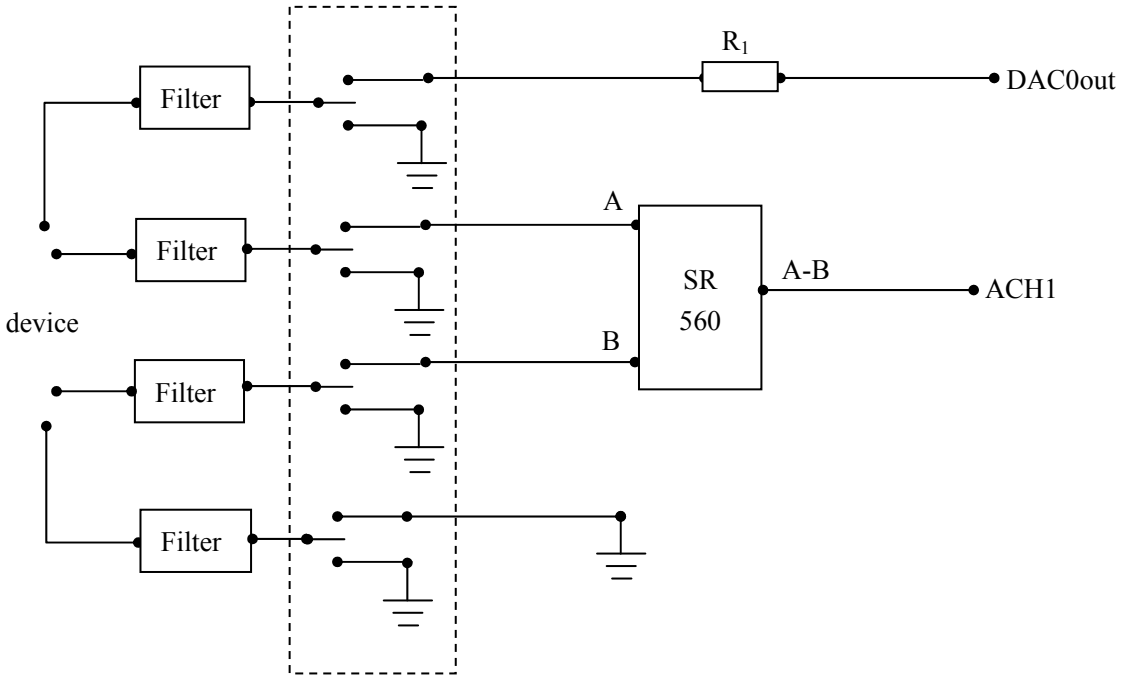

Fig. III-8. circuit diagram of four-probe DC current bias measurement

In the four probe current-bias measurement, most of voltage drop is on the resister R_1, the value of which is chosen to be much more lager than device resistance, such as 10M Ω or 100M Ω. It is equivalent to a current source after the voltage is applied onto the large resister. The current reaches the device from one lead of the outer pair, and passes the device and flows to ground on the other outer lead. The voltage signals of the inner pair are taken by SR560 at channel A and B, subtracted and amplified, then read by channel ACH1 on the BNC interface. The pair of input cables A and B should be twisted or braided together for eliminating any pickup of the noises from

the electromagnetic environment.

Two probe AC voltage bias is used for device conductance measurement, such as $G(V_g)$, $G(V)$ or $G(V_g,V)$ measurement. The circuit diagram is shown in the following figure.

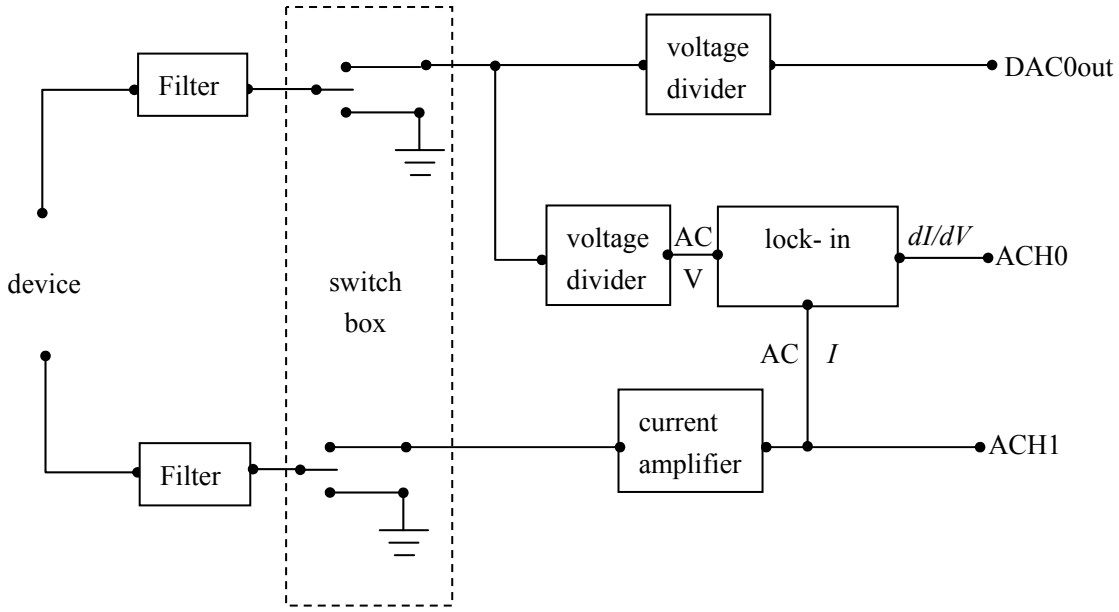

Fig. III-9. circuit diagram of two-probe AC voltage bias measurement

The DC voltage from interface is mixed with small AC reference voltage from lock-in amplifier, and applied across the device. Then the current signal is amplified by current amplifier and fed back to lock-in, which extracts the current signal with the same frequency to the reference voltage signal based on the orthogonality of sinusoidal functions, and output to channel ACH0. The output of the lock-in amplifier is directly proportional to *dI/dV.* Typically a resistance calibration using known

resistors is necessary before real measurement. Sometimes we also need to compare the value of device conductance with two probe *I-V* curves, to make sure the signal is not suppressed by the filter at a particular frequency.

Reference

Deshpande, V.V., *et al*., Nature Physics, 2008. 4(4):314.

Jarillo-Herrero, P., *et al*., Nature (London) 2006, 439, 953.

Kong, J., *et al*., Nature (London) 1998, 395, 878.

Chapter IV.

Gate-Tunable Dissipation and "Superconductor-Insulator" Transition in Carbon Nanotube Josephson Junctions

IV-1. Introduction

The interplay among dissipation, disorder, and fluctuations has been the focus of much theoretical work (Herrero *et al*., 2002, Refael *et al*., 2003, Wilhelm *et al*., 2001, Glazman *et al*., 1997, Chakravarty *et al*., 1986, Goswami *et al*., 2006, Hoyos *et al*., 2007, Fu *et al*., 2006) in quantum bosonic systems. In particular, superconductor-insulator transitions (SITs) observed in single Josephson junctions (JJs) (Penttila *et al*., 1999), nanowires (Bezryadin *et al*., 2000, Lau *et al*., 2001), two-dimensional (2D) JJ arrays (Rimberg *et al*., 1997), and 2D thin films (Mason *et al*., 1999) have been attributed to changes in dissipation. However, dissipations in these systems are typically determined by device geometry and/or shunt resistors and cannot be tuned in situ; thus direct tests of theoretical predictions are not straightforward because of the inevitable variations in mesoscopic devices. Though dissipation and SIT via in situ control were reported in 2D JJ arrays fabricated on semiconductor heterostructures (Rimberg *et al*., 1997) and more recently in atomic Bose-Hubbard (McKay *et al*., 2008) systems, such phenomena were not observed or examined in detail for a single JJ, the simplest Josephson system.

We observed gate tunable dissipation and evidence for "superconductor insulator

transition" in a single wall carbon nanotube JJ (Buitelaar *et al*.,2003, Buitelaar *et al*., 2002, Jorgensen *et al*., 2007, Tsuneta 2007, Cleuziou *et al*., 2006, Cleuziou *et al*., 2007, Morpurgo *et al*., 1999, Kasumov *et al*., 1999, Eichler *et al*., 2007, Jarillo-Herrero *et al*., 2006). As the device tuned by the gate from resonance to anti-resonance energy level, the value of super current passing through the device changes from maximum to minimum, while the current-voltage (*I-V*) curve changes from non-hysteretic to hysteretic. It indicates that the junction is tuned from overdamped junction to under damp junction, in agreement with the resistively and capacitively shunted junctions (RCSJ) model. As the Fermi level is tuned to a local resistance maximum, we observed a "superconductor insulator transition" with a critical normal state resistance (R_N) ~10 kΩ. Our results demonstrates the continuous tune of dissipation in individual JJ and is the first observation in a gate tunable SIT in a single JJ. Such SWNT JJs will enable *in situ* study of the interplay between dissipation and quantum coherence, and have implications for implementing quantum computation in superconducting systems.

IV-2. Introduction to RCSJ Model

Before the main content of this chapter, we need to introduce the background theory about resistively and capacitively shunted junctions model (Tinkham 1996), because this model is frequently referred in this chapter.

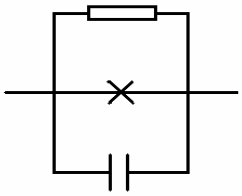

Fig. IV-1. schematics of RCSJ model

JJ can be modeled by three parallel channels: superconducting channel, resistive channel and capacitive channel. The current passing through JJ is the sum of current component in each channel, given by

$$I = I_c \sin\Delta\varphi + V/R + CdV/dt \qquad (1)$$

Simplify the formula, then we get

$$\Rightarrow \frac{d^2\Delta\varphi}{d\tau^2} + Q^{-1}\frac{d\Delta\varphi}{d\tau} + \sin\Delta\varphi = \frac{I}{I_c} \qquad (2)$$

Where $\tau = \omega_p t$, $\omega_p = (2eI_c/\hbar c)^{1/2}$, $Q = \omega_p RC$

The simplified formula can be understood as a "tilted washboard" model: a particle of mass $(\hbar/2e)^2 C$ moving in an effective potential $U(\Delta\varphi) = -(\hbar/2e)\cos\Delta\varphi - (\hbar I/2e)\Delta\varphi$, which is titled by the current bias. Considering frictionless (no dissipation) case at zero temperature, the particle is trapped by the local minimum of effective potential, that is, it is in the superconducting state, until the bias voltage reaches the critical current value. Once

the particle starts to roll down along the effective potential, the phase coherence is broken, resulting in transition from supercurrent into resistive regime ($V \sim d(\Delta\varphi)/dt$).

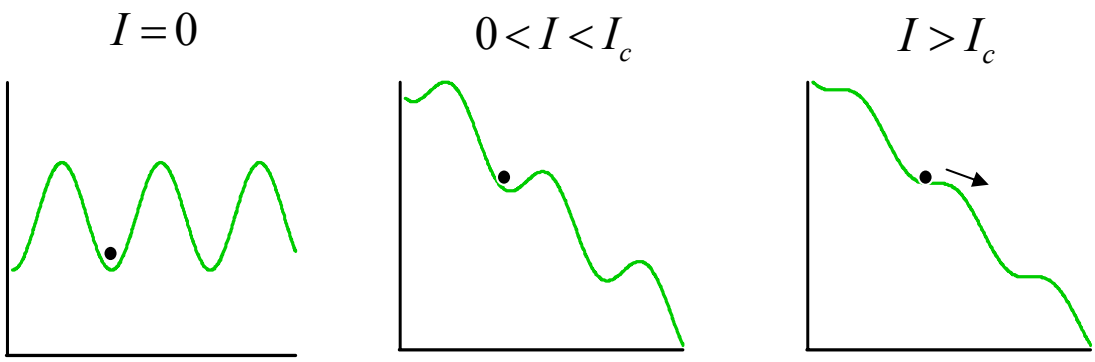

Fig. IV-2. “tilted washboard” model

With small dissipation (under damp junction), the board must be tilted more than frictionless I_C to start rolling of particle, while the motion can be stopped with board more tilted back ($I_c > I_r$) due to the momentum of the particle, resulting in the *I-V* curve hysteresis. In comparison, with large dissipation (overdamped junction), the particle starts and ends motion with large friction at the same tilted slope $I_c = I_r$, display non-hysteresis *I-V* curve.

Considering the thermal fluctuation in the under damp junction, the I_c decreases and I_r increases, because thermal excitation can excite the particle jump out of the local potential minimum, resulting in reduction of hysteresis size.

IV-3. Experiment Preparation

The devices are fabricated as the description as the pervious chapter. We just emphasis, that the wafer is highly doped Si substrates with a 300-nm thick SiO_2 dielectric layer and contact electrodes are made of 5nm Pd and 80 nm Al. Fig. IV-3a is SEM picture similar to the devices we measured.

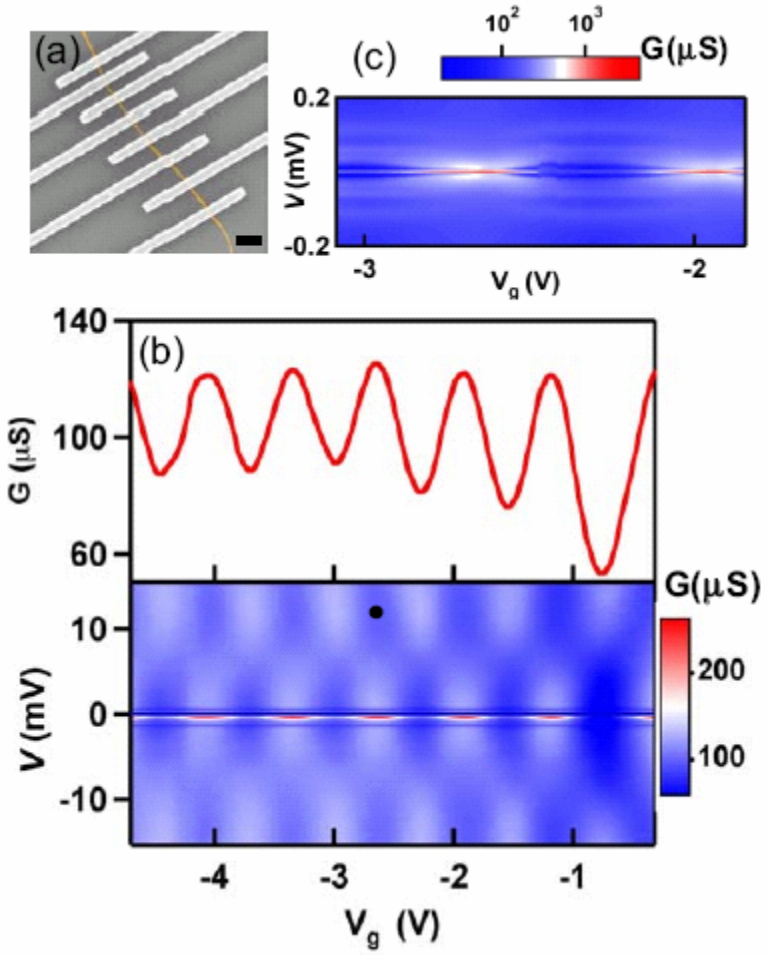

Fig. IV-3. (a). SEM graph of a nanotube (gold) connected to 8 electrodes (white). Scale bar: 400 nm. (b) Upper panel: Normal state conductance of a SWNT device as a function of V_g at 260mK. Lower panel: Differential conductance vs bias V and gate voltages V_g. (c). High resolution plot of dI/dV vs V and V_g at small biases. Notice the logarithmic color scale.

IV-4. Differential *G* Spectroscopy

The differential conductance G as a function of bias voltage (V) and gate voltage (Vg) at 260mK is plot in Fig. IV-3b lower panel, where the striking checker-board pattern indicates the signature of Fabry-Perot interference of electron waves in the nanotube. The differential conductance varies from maxima to minima, corresponding to the device tuned from resonance to anti-resonance transmission via discrete energy levels, which arise from the finite length of the nanotube (Liang *et al*., 2001). The characteristic energy scale of oscillation can be estimated from the value bias voltage, at which the differential conductance reaches the first maximum, and yields the level spacing $hv_F/2L$ where $v_F \sim 10^6$ m/s is the Fermi velocity, and L is the distance traveled by charges between successive reflections. From Fig. IV-3b, we obtain $V_c \approx 11.8$mV, suggesting $L \approx 175$ nm. The excellent agreement with the real source-drain electrodes separation 180 nm, indicates the scattering only occurs at the nanotube-electrodes interfaces and the nanotube is ultra clean. Fig. IV-3b upper panel is a conductance - gate voltage curve taken at 0.7mV to exclude the superconducting proximity effect. The magnitude of normal state conductance sinusoidally oscillates between 80 and 125μS, which is approaching the theoretical value of a perfectly coupled nanotube, $G_Q=4e^2/h \approx 160$ μS. (here e is the electron's charge and h is the Planck's constant). These data indicate that our SWNT devices are clean, well-coupled to electrodes, and support ballistic and phase coherent charge transport.

At zero bias voltage, we observed the dramatically enhanced conductance peaks arising from the superconducting proximity effect. The magnitude of the peaks

reaches a few mS >> G_Q, indicating the presence of a supercurrent. In the high resolution sweep Fig. IV-3c, a few more conductance peaks are next to the center peaks at sub-harmonic multiples of 2Δ(Δ is the superconducting energy gap of Al). These peaks arise from multiple Andreev reflections (MAR) of charges at the superconductor-SWNT interfaces (Buitelaar *et al*., 2003, Octavio *et al*., 1983, Buitelaar *et al*., 2002), and suggest an estimated $2\Delta \sim 240$ μeV. To investigate a supercurrent, we move into *I-V* measurement.

IV-5. *I-V* Characteristics

V-I measurement is performed by four-probe current bias, which has been described in the previous chapter. Two outer electrodes are the current source and drain, while the voltage difference is taken between the inner two electrodes. At small current bias I <~nA, a supercurrent is observed ~nA, with zero or finite voltage. When the current bias exceed the critical current I_c, the device switches from supercurrent branch to resistive branch, with a slope approaching the local normal state resistance at high biases. More interestingly, the *V-I* characteristics dramatically varies with the gate voltage, resulting from the tuning of the electrodes' Fermi levels with respect to the quantized energy levels in the nanotube. Fig. IV-4a plots three representative *V-I* curves α, β and γ at different gate voltage, where the device is tuned at off-resonance, intermediate and on-resonance transmission, respectively.

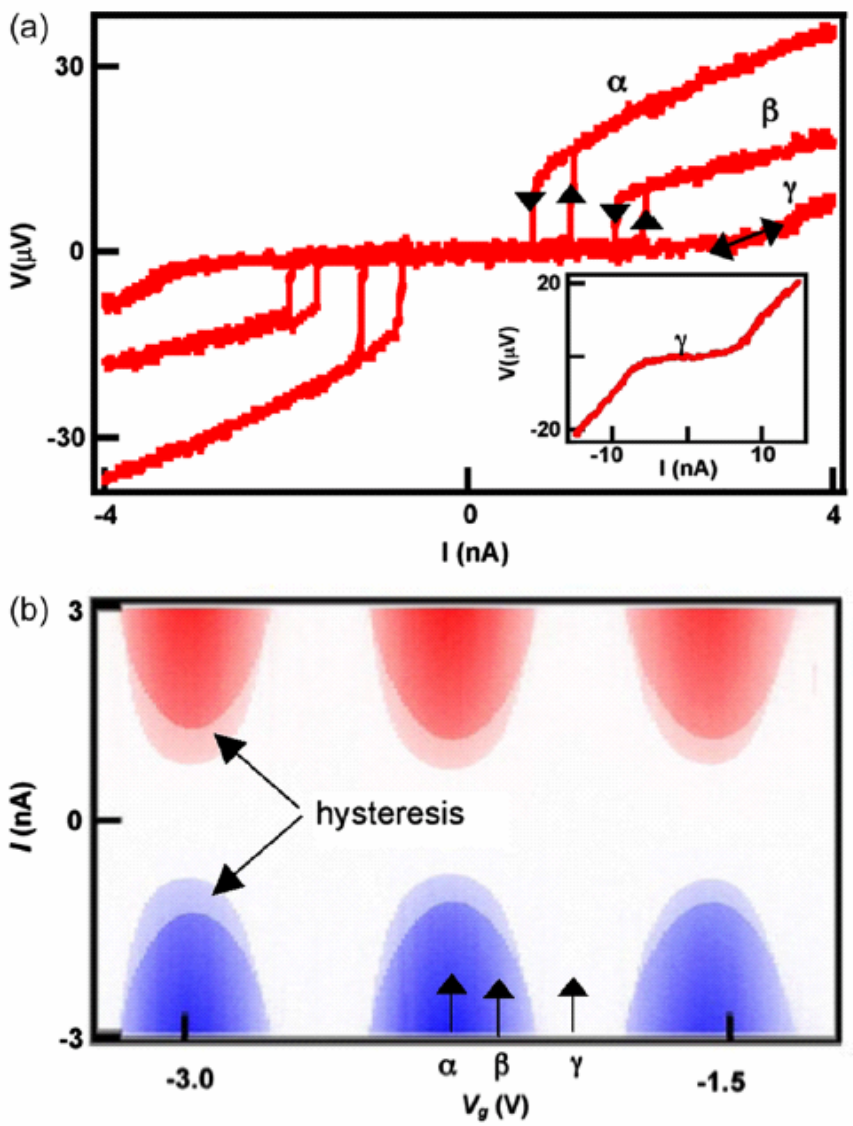

Fig. IV-4. (a). *V-I* characteristics of a S/SWNT/S device at 260mK at 3 different V_g. Inset: γ curve at large current bias. (b) Measured voltage across the device vs I and V_g, indicating transition from supercurrent (white) to resistive (blue/red) states. α, β and γ indicate the gate voltages at which line traces in (a) are taken. The figure consists of data taken in both up-sweep and down-sweep directions, which are set to be 50% transparent and superimposed together to accentuate the gate-dependent hysteresis (pale blue and pale red).

In a JJ with discrete energy level and 2 spin degeneracy system, the critical current at wide resonance regime can be estimated by

$$I_c \approx \frac{2e\Delta}{\hbar}\tanh\left(\frac{\Delta}{2k_BT}\right)\left[1-\sqrt{1-\frac{G_N}{4e^2/h}}\right] \quad (1)$$

where the term in the square brackets takes into account of the asymmetric coupling between the SWNT and the two electrodes, and k_B is Boltzman's constant. Our device with extrinsic level widths $\Gamma >\sim$ meV (Beenakker *et al*., 1992) can be explained by the formula, which suggests that the critical current increases with increasing G_N. From Fig. IV-4a we find out that *V-I* curves γ has largest critical current 8.3nA, where the device is at resonance state with a local conductance maximum, while *V-I* curves α has the smallest critical current 1.1nA, where the device is at resonance state with a local conductance minimum. the value of I_c is taken at that of the largest slope *dV/dI*.

The gate dependence of I_c has been reported in a few publications (Buitelaar *et al*.,2003, Buitelaar *et al*., 2002, Jarillo-Herrero *et al*., 2006, Tsuneta 2007, Cleuziou *et al*., 2006, Cleuziou *et al*., 2007, Morpurgo *et al*., 1999, Kasumov *et al*., 1999, Eichler *et al*., 2007, Beenakker *et al*., 1992), but another unexplored aspect is the shape of the *V-I* curve, which contains a wealth of information on the junction dynamics. In the RCSJ model, the *V-I* curve of an under damp junction in the strong coupling regime ($E_J >> k_BT$) is hysteretic, displaying shape switching points between supercurrent branches and resistive branches, and the upward switching point (critical current) I_c is larger than the downward switching point (retrapping current) I_r ($I_r \leq I_c$). Here $E_J = \frac{\hbar I_c}{2e}$ is the Josephson coupling energy. At finite temperatures, thermal fluctuations reduce I_c but increase I_r, thereby reducing the hysteresis size, until $I_r = I_c$ at

E_J<~k_BT. In the overdamped junction, the transition between supercurrent and resistive branches is always smooth and at the same critical current value (non-hysteretic). Thus, hysteresis observed in the *V-I* characteristics, is an important indication of the junction dynamics, as well as the relative magnitudes of Josephson coupling to thermal fluctuations.

In Fig. IV-4a, *V-I* curves α is taken at center of an anti-resonance regime, and display sharp switch at I_r and I_c, with the largest hysteresis and small I_c value. *V-I* curves β is at intermediate regime, and has small hysteresis. Both of them resemble the under damp junction characteristics. In contrast, *V-I* curves γ from the resonance regime has largest I_c value, with smooth transition and no hysteresis, which is typical behavior of overdamped junction. *V-I* curves on a large range of gate are plot in Fig. IV-4a, where the upward and downward sweep are overlapped and the latter is in 50% color scale for better presence of difference between two sweep. In the plot, white region is the supercurrent branches, while the blue and red regions are the positive and negative resistive branches respectively. The hysteresis appears as the pale blue and pale red regions, bounded by the values of I_c and I_r, with sizes that change with V_g. By examining the variation of the *V-I*, device is tuned by gate from resonance to anti-resonance, with supercurent from maximum to minimum, and the shape of *I-V* from hysteresis to non-hysteresis. The trend is periodically observed over a large range in V_g.

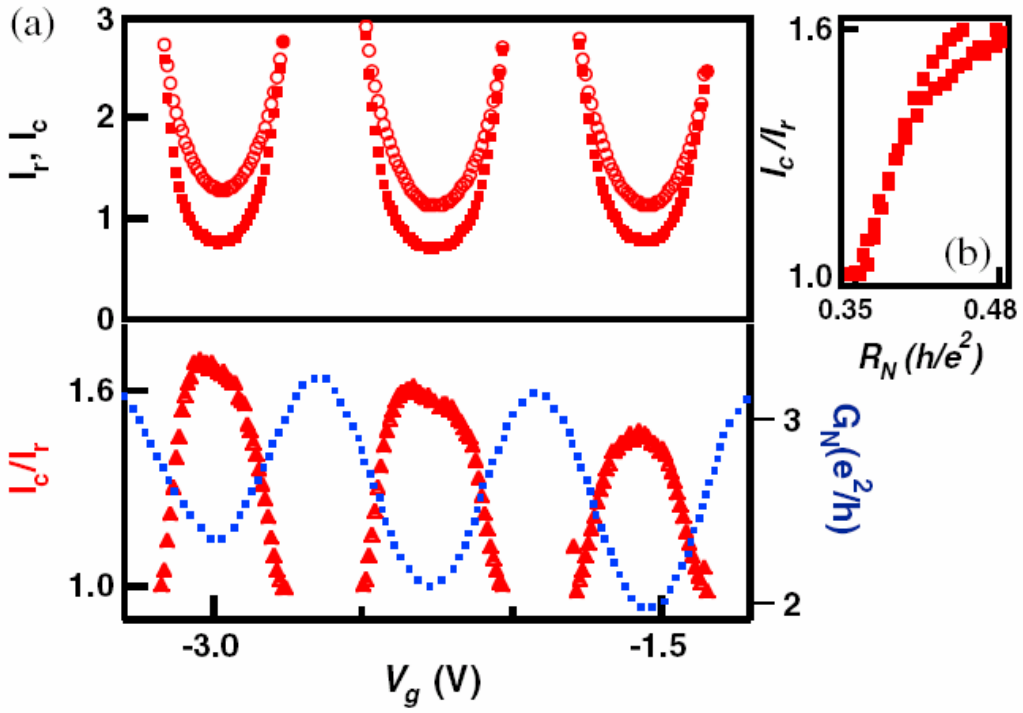

Fig. IV-5. (a). Upper panel: I_c (open circles) and I_r (closed circles) vs V_g. Lower Panel: I_c/I_r (triangles, left axis) and G_N(dotted line, right axis) vs V_g. (b). I_c/I_r vs R_N for V_g =-2 to -2.5V.

A quantitative analysis is presented in Fig. IV-5. The upper panel plots I_c (open circles) and I_r (closed circles) as a function of gate voltage, and the lower panel plots ratio of I_c and I_r (triangles) and G_N (dotted line, right axis) vs V_g. Clearly, the size of hysteresis anti-correlates with size of I_c and G_N. I_c/I_r reach up to ~1.7, when I_c is at local minimum ~1.3nA and as well G_N is at local minimum ~$2e^2/h$. however, we expect the size of hysteresis correlates with E_J/k_BT, so the largest hysteresis should occur at the resonance regions. Our experimental result is completely opposite to the expectation. On the other hand, in the RCSJ model dissipation can be parameterized by $1/Q$, where Q is the junction's quality factor, given by

$$Q=\omega_p R_j C_j, \qquad (2)$$

where $\omega_p = \sqrt{\frac{2eI_c}{\hbar C_j}}$ is the plasma frequency, R_j and C_j are the shunt resistance and capacitance of the junction, respectively. If Q>1, the junction is under damp. In our system, R_j is given by the R_N ~ 10 kΩ and C_j is obtained by capacitance from the gate to device ~0.2 fF, then we have Q~1.3. so the device is under damp junction and closed to the transition to the overdamped junction. At T=0, Q is related to the ratio I_c/I_r by

$$I_c / I_r = \pi Q / 4 \qquad (3)$$

The ratio reduces with the thermal fluctuation, but in general the dissipation can be estimated by I_c/I_r. Combining formula (1)~(3), we obtain I_c/I_r is roughly proportional to the $\sqrt{R_N}$, which is consistence with the experimental result as directly indicated in Fig. IV-5c. So the results show that the gate tunable dissipation in the SWNT JJ increases with R_N.

IV-6. Superconductor-Insulator Transitions

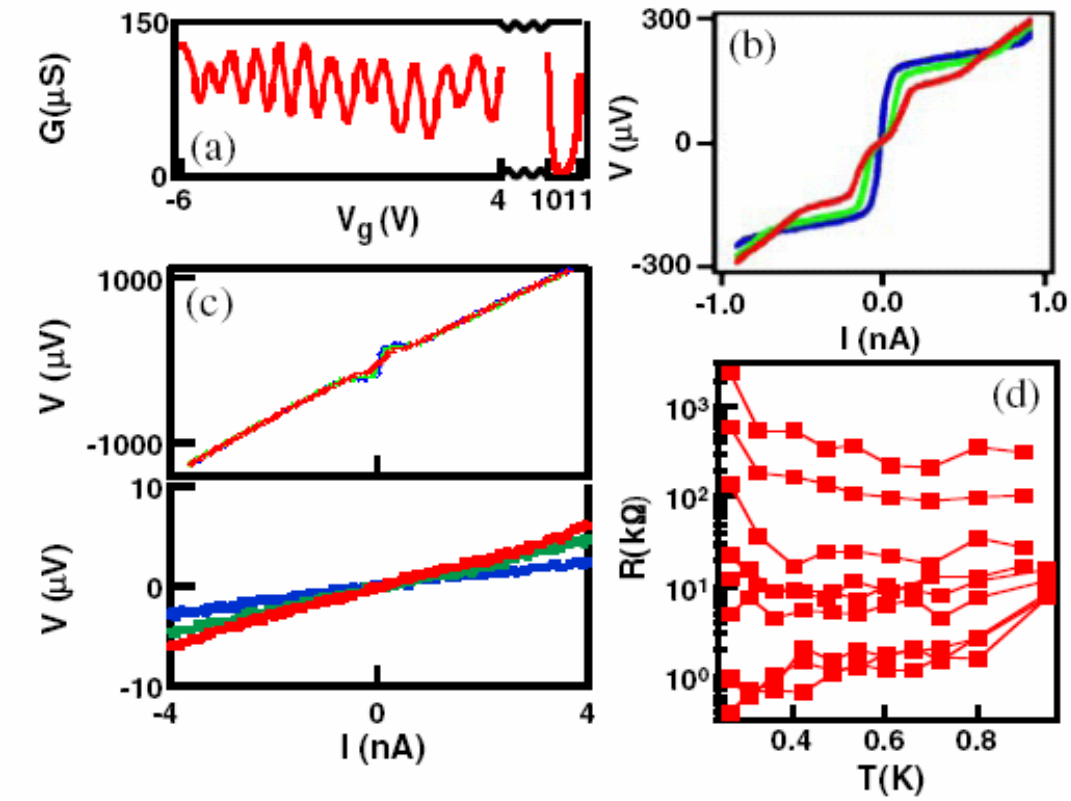

Fig. IV-6. (a). G_N vs V_g for a device with a conductance minimum at V_g ~10.5V. (b). *V-I* characteristics at V_g=10.5V at T=0.7K (red), 0.5K (green) and 0.26K (blue). (c). Upper Panel: same as (b) with larger bias range. Lower panel: *V-I* curves at V_g=-0.51V at T=0.9K (red), 0.53K (green) and 0.26K (blue). (d). R_0 vs T at different V_g (from top to bottom, V_g = 10.5, 10.72, 10.83, 11, -0.81, -0.71, -0.61, -0.58 and -0.55 V).

In a gate tunable dissipation in a SWNT JJ, superconductor insulator transition is possibly observed. Especially, at sufficient small G_N, low dissipation may give rise to delocalization of superconducting phase, such as insulator phase. The characteristic of insulator phase is that at the low temperature and low bias resistance decreases to R_N, with increasing temperature. Such transition is observed in our device 2, which is 190nm separation device. The device behaves similarly with the data present in the above sections, including regular Fabry-Perot patterns, MAR features which yield

$2\Delta \sim 200$ μeV, and gate-tunable hysteretic *V-I* characteristics, except at $V_g \sim 10.5$V the normal state resistance reach a low value $G_N \sim 3$μS (Fig. IV-6a). Such a resistive state may arise from the presence of a small band gap. There the *I-V* around zero bias at low temperature (the blue curve in Fig. IV-6b) is dramatically different in the slope of $3\text{M}\Omega >> R_N$, and the slope decreases to R_N, when the current bias is swept beyond $2\Delta \sim 210$ μeV. The negative *dR/dI* behavior resembles that of the insulating phase or an S-I-S junction, in stark contrast with the typical *V-I* characteristics of a superconducting junction as indicated in Fig. IV-4. The temperature dependence investigation verifies the insulator phase. Within the gap, more *V-I* are plot in Fig. IV-6b T=0.7K (red), 0.5K (green), showing that the zero bias resistance decreases with increasing temperature, but the resistance outside the superconducting gap 2Δ stays the same $\sim R_N$. These behaviors verify that the junctions stay metallic and insulator phase arise from the superconductivity.

Further evidence for the transition is given by the zero bias resistance temperature dependence study at a series of gate voltages with different R_N, as shown in Fig. IV-6d. At the T=1K, all of the *I-V* are linear, so zero bias resistance equals R_N. When temperature drops, the trend at different gate voltage with different R_N diverge into three cases. The state with high $R_N > 20\text{k}\Omega$, R_0 decreases with temperature. In contrast, the state with high $R_N < 8\text{k}\Omega$, R_0 increases with temperature. With intermediate R_N, R_0 are almost constant with temperature. Thus the junction may be superconductor-like or insulator-like, depending on a "critical" value of $R_N \sim 8$-20 kΩ.

Such behavior is reminiscent of the dissipation-driven SIT observed in 2D superconducting thin films and JJ arrays, where the transition occurs when the sheet resistance is equal to $h/4e^2$~6.5kΩ (Goldman *et al*., 1998, Penttila *et al*., 1999, Rimberg *et al*., 1997). In the context of gate tunable dissipation described in the first part of the letter, the SIT is likely driven by modulations in dissipation, though the detailed dynamics and dissipation mechanism warrant further experimental and theoretical investigation.

IV-7. Phase Diffusion

In traditional and nanotube JJs, the thermal and electromagnetic environments play an important role in determining the junction dynamics, which is usually described within the resistively and capacitively shunted junction (RCSJ) model as we introduced in the section II of this chapter. Here the phase difference across the junction is visualized as a particle localized in, or running down, the tilted washboard potential, corresponding to the supercurrent-carrying state and the resistive state of the junction, respectively. For short ballistic SWNT JJs, the superconductors are coupled via a single quantized energy level; in the strong Josephson coupling regime $E_J >> k_BT$, these devices behave as under damp junctions, with premature switching from supercurrent to resistive branches induced by the electromagnetic environments (Jarillo-Herrero *et al*., 2006). In contrast, in the intermediate to weak Josephson coupling regime $E_J <\sim k_BT$, long diffusive MWNT JJs can be described by phase

diffusion down the tilted washboard potential.

In this section, we present measurements on short ballistic SWNT devices that are well-coupled to the electrodes (hence with negligible charging energies), but in the phase diffusion regime: we observed Fabry Perot interference, multiple Andreev reflections (MAR), and gate-tunable voltage current (*V-I*) characteristics. Each *V-I* curve exhibits a sharp switching from the supercurrent to the quasiparticle branches, and the measured switching current ranges from 65 pA to 2.5 nA. In contrast to a previous report in the reference (Jarillo-Herrero *et al*., 2006) and in the above sections, we find that both the magnitude of the switching current and the finite resistance observed in the supercurrent branch are in good agreement with the classical phase diffusion model in the weak Josephson coupling regime (Tsuneta *et al*., 2007, Tinkham 1996, Martinis *et al*., 1989, Ingold et al., 1994). Our results demonstrate that (quasi)ballistic, weakly coupled SWNT Josephson transistors are strongly affected by dissipation determined by the small impedance of the biasing circuit at high frequencies. We also note that our results are obtained at 300 mK, indicating that ultra low temperatures are not required for observing supercurrent in SWNT JJs.

The devices preparation and measurements are similar to the process described in the above sections. This section presents results from two different devices: Device 1 with a Pd (6 nm)/Al (70 nm) bilayer, and source-drain separation of 390 nm; Device 2 with a Pd (3 nm)/Al (70 nm) bilayer, and separation of 580 nm. The gate dependence of room temperature resistance indicates that both SWNTs are small band

gap semiconductors.

In the high magnetic field ($H=8\ T$), the differential conductance plot of Device 1 as a function of source-drain voltage V and gate voltage V_g, shows the FP interference "checker-board" pattern. And the dimension estimated from the characteristic voltage scale, matches the source-drain spacing, which indicates devices can be considered to be relatively free of defects and to have almost ohmic contacts. In contrast, the nanotube in Device 2 is quasiballistic with the presence of only a few scatterers.

We now focus on the device behavior with superconducting electrodes at $H = 0$. At $|V|\geq 50$ μV, transport was dominated by the quasiparticles and the FP interference pattern persisted. At small biases $|V|\leq 50$ μV, the transport characteristics in both devices changed dramatically: conductance peaks were observed, persisting through all gate voltage ranges, indicating enhanced transport through resonant and off-resonant states. For Device 2 with its thinner Pd contact layer, we observed giant zero-bias conductance, which reached as high as 10 e^2/h, much larger than G_0, indicative of a superconducting proximity effect (Fig. IV-7). At finite but small biases, several pronounced conductance peaks were observed. We identify $2\Delta/e = \pm 0.18$ mV, where the conductance peaks at 2Δ correspond to the onset of direct quasiparticle transport (Δ is the superconducting gap of Al). The peaks at $V\leq\pm 0.09$ mV result from MAR processes (Andreev 1964). During an Andreev reflection, an incident electron at the SWNT/S interface is reflected as a hole, with the formation of a Cooper pair in a superconducting condensate. For a S/SWNT/S junction, an electron can be reflected

back and forth between the electrodes several times, each time gaining energy eV, before it gathers sufficient energy to exit the SWNT as a quasiparticle into the superconductor. MAR processes give rise (Blonder *et al.*, 1982) to features in dI/dV at voltages which are subharmonic multiples of 2Δ, and contribute to the giant conductance peak at zero-bias. As shown in Fig. IV-7, the MAR features persist throughout the whole range of measured gate voltage, with the position of peaks fluctuating slightly with changing V_g.

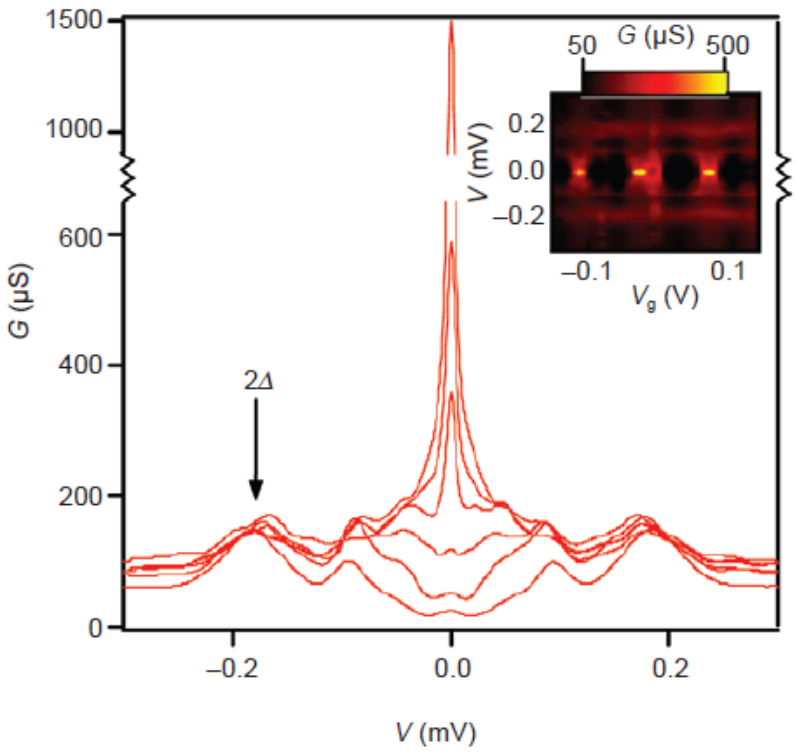

Fig. IV-7. Plot of conductance G vs bias voltage V for Device 2 at V_g=0.024, 0.044, 0.002, –0.041, –0.038, and -0.029 V (from bottom to top at V=0). The inset shows the MAR features, plotting G as a function of bias and gate voltages.

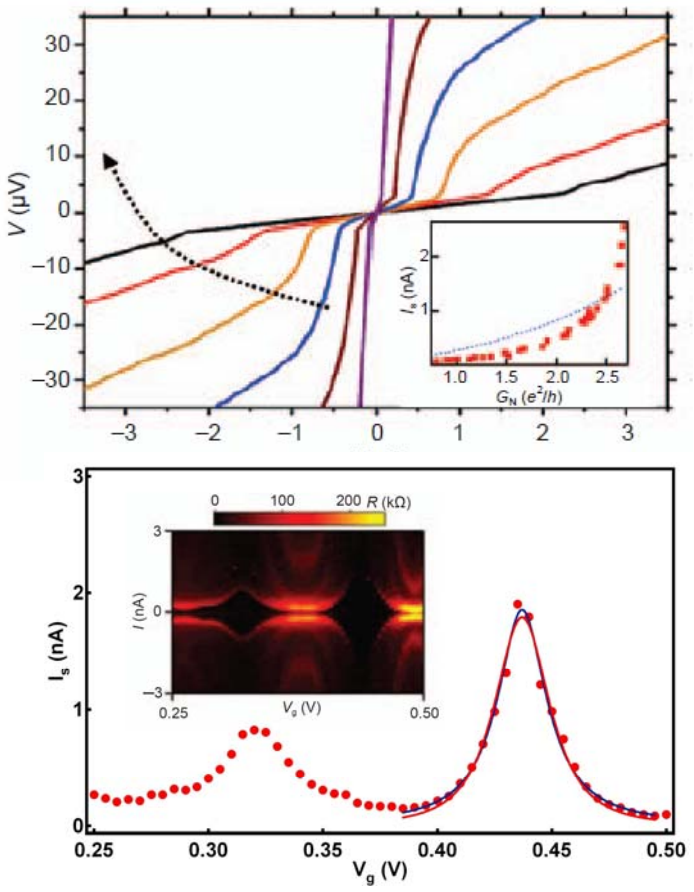

Fig. IV-8. (a) *V-I* characteristics showing the modulation of the switching current is with values of V_g (increasing in the direction of the arrow) of 0.485, 0.479, 0.473, 0.467, 0.445 and 0.440 V. The inset displays a plot of the switching current vs normal state conductance G_N. The dotted line is a best fit to Eq. (5a) with the fitting parameter Ic= 5.2 nA. (b) Plot of switching current vs gate voltage at two resonant states. The blue and red lines are the fitting lines on a individual resonance. The differential resistance plot is shown in the inset.

To investigate the possibility of a supercurrent, we current-biased the devices and the resulting dc *V-I* characteristics are shown in Fig. IV-8(a). At low current *I* (below the order of nA), the devices remain on the supercurrent branch and display finite (and typically small) linear response resistance R_0; when the bias current exceeds a threshold, is, the measured voltage abruptly switches to the quasiparticle branch, with

a resistance that approaches R_N, the normal state resistance of the junction. The *V-I* characteristics are strongly gate-dependent: both the switching current, I_s, and linear response resistance R_0 can be modulated by V_g, and are correlated with the normal state conductance G_N (Fig. IV-8(a) inset, Fig. IV-8(b)). For instance, for the V_g range 0.44–0.536 V, G_N decreases from $2.68e^2/h$ to 0.8 e^2/h, I_s decreases from about 2.5 nA to 65 pA, while R_0 increases from about 1.5 kΩ up to 44 kΩ. Moreover, there exists a simple relationship between I_s and R_0. In a log–log plot of I_s and R_0, (Fig. IV-9 inset) the data points fall on a straight line, indicating a power-law dependence. The solid line is a best fit curve to $I_s = A/R_0$, with the value of coefficient A being ~3200 nA·Ω.

The conductance through a single discrete energy level is given by $G_N = (4e^2/h)T_{BW} = (4e^2/h)(\Gamma_1\Gamma_2/((V_g - V_{gr})^2 + 0.25(\Gamma_1+\Gamma_2)^2))$, where T_{BW} is the Breit–Wigner transmission probability, Γ_1 and Γ_2 are the tunnel rates through the each barrier, V_{gr} is the resonance gate voltage. As for the device2, the maximum conductance is 2.68 e^2/h, yielding the a barrier asymmetry $\Gamma_1/\Gamma_2 \approx 0.256$. With the value of the barrier asymmetry, we performed the $I_s(V_{gate})$ fitting based on the relation of $I_c = I_{c0}[1-(1-(\Gamma_1\Gamma_2/((V_g - V_{gr})^2 + 0.25(\Gamma_1+\Gamma_2)^2)))^{1/2}]$, where the resonance gate voltage is set at 0.437 V, and all value of gate voltages are converted into energy scale by the gate efficiency. As indicated in the blue line of Fig. IV-8(b), we obtain the reasonable fitting parameters as Γ_1=0.414 meV/h, Γ_2=1.64 meV/h, I_0=4.64 nA. Considering the phase diffusion, the switching current becomes much smaller than the theoretical value, as $I_{CM} \propto I_C^{3/2}$ (see discussion below). So we fit the $I_s(V_{gate})$ with the

relation of $I_{CM} = I_c[1-(1-(\Gamma_1\Gamma_2/((V_g - V_{gr})^2 + 0.25(\Gamma_1+\Gamma_2)^2)))^{1/2}]^{3/2}$ as shown in the red line of Fig. IV-8(b), and obtain the Γ_1=0.591 meV/h, I_0=7.08 nA, which reasonably agree with the parameters from the first fitting (see below, however, for discussion on why this simple formula does not provide good fits for $I_s(G_N)$).

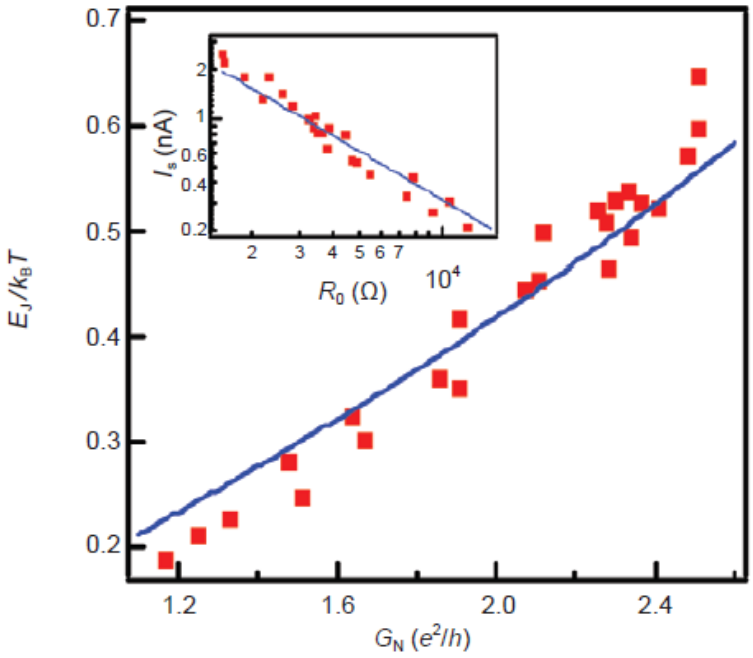

Fig. IV-9. Main panel: a plot of E_J/k_BT (see text) vs normal state conductance. Red squares are data points and the solid line is a fit to Eq. (8). Inset: Plot of switching current vs zero bias resistance. Red squares are data points and the solid line is fit to the data using $I_s = A/R_0$, where A is a fitting parameter, determined to be 3200 nA·Ω

Gate-tunable *V-I* characteristics and supercurrent have been observed (Jarillo-Herrero *et al.*, 2006, Tsuneta *et al.*, 2007) in SWNTs, arising from resonant and off-resonant transport across quantized single particle level in a finite SWNT segment. Theoretically (Beenakker *et al.*, 1992), for two superconductors symmetrically coupled via discrete energy levels in a 2-channel quantum dot, the

maximum critical current in the wide resonance regime (I >>Δ) is

$$I_c \approx \frac{2e\Delta}{\hbar}\tanh\left(\frac{\Delta}{2k_BT}\right) \qquad (4)$$

where T=300 mK is the temperature, Γ~1 meV is the level broadening due to the finite lifetime of the electron, *e* is the electron charge. For Device 2, $2\Delta \sim 0.18$ meV as determined from the MAR features, yielding $I_{c0} \sim 41$ nA. In actual devices, the asymmetric coupling is expected to decrease the measured normal state conductance G_N, which in turn leads to a reduction in the actual critical current, given by

$$I_c \approx I_{c0}\left[1-\sqrt{1-\frac{G_N}{4e^2/h}}\right] \qquad (5)$$

The maximum value of G_N is 2.68 e^2/h for Device 2, and thus we expect the critical current to be as large as ~17.4 nA. This value is nearly an order of magnitude larger than the observed value of 2.5 nA. This large discrepancy cannot be accounted for by the presence of disorders, since in this case I_c would be expected (Beenakker 1992) to be lower but remain on the same order of magnitude as given by Eq. (5).

To understand the inverse relationship $I_s \propto R_0^{-1}$ and the large discrepancy between theoretical and experimental values of the critical current, we focus on the dynamics of the SWNT Josephson junction within the RCSJ model. The dc *V-I* characteristics of the devices are consistent with that of under damp junction. In this case, small fluctuations from the thermal or electromagnetic environment leads to premature switching of the junction into the "running" or resistive state, yielding (Jarillo-Herrero

et al., 2006, Joyez *et al*., 1994)

$$I_s \approx I_c \left[1 - \sqrt{1 - \frac{G_N}{4e^2/h}} \right]^{3/2} \qquad (5a)$$

Equation (5a) can qualitatively account for the monotonic decrease in I_s with G_N. However, fitting the data $I_s(G_N)$ to Eq. (5a) results in poor quantitative agreement (Fig. IV-8(a) inset, dotted line). Thus the simple picture of premature switching in under damp junctions does not adequately account for our data.

Here we show that the observed behavior can be quantitatively described by the classical phase diffusion model (Martinis *et al*., 1989, Ingold et al., 1994). In the phase diffusion regime, the junction dynamics depends crucially on the impedance Z of the biasing circuit at the characteristic plasma frequency of the JJ. Since the junction is not isolated from its electromagnetic environment, Z is typically on the order of the impedance of free space (377 Ω) (the exact value of Z depends on the detailed circuit configuration). Hence, even though the junction is under damp at low frequencies, it is overdamped at high frequencies, which causes the "particle" (i.e., the relative phase across the junction) to diffuse (instead of running) down the tilted washboard potential. This leads to a finite voltage measured in the nominally zero resistance state, yielding a zero-bias resistance

$$R_0 \approx \frac{Z}{I_0^2(E_J / k_B T) - 1} \qquad (6)$$

where $E_J = hI_c/2e$ is the Josephson coupling energy of the junction, Z is the

environmental impedance at ac, and $I_0(x)$ is the modified Bessel function. For Device 2, the upper limit of E_J is estimated to be ~ 0.036 meV for I_c ~ 18 nA, comparable to the thermal energy k_BT ~ 0.025 meV at 300 mK. We thus consider the weak Josephson coupling regime of $E_J<k_BT$, where Eq. (6) is simplified to

$$R_0 \approx 2Z(\frac{k_BT}{E_J})^2 \qquad (7)$$

and the switching current is given by $I_s= eE_J^2/2k_BTh$. Combining the two equations yields $I_s= eZk_BT/hR_0$. Thus, I_s is proportional to R_0^{-1}, in agreement with our experimental observation (Fig. IV-9 inset). Substituting the fitting coefficient A=3200 nA·Ω into eZk_BT/h, gives a value of Z ~ 485 Ω, which is a reasonable value. (Here five data points with $R_0>R_N$ were excluded from the fitting, because the large values of R_0 indicate reduced quasiparticle conductance due to the formation of the superconducting energy gap in the density of states, where Eqs. (6) and (7) are inapplicable.)

Further insight is provided by investigating the dependence of R_0 on G_N at different gate voltages. For each V_g , we first calculate the ratio E_J / k_BT by solving Eq. (6) numerically using the measured values of R_0 and Z=485 Ω. The calculated values of E_J / k_BT are then plotted against G_N (in units of e^2/h) in Fig. IV-9. From Eq. (5), we expect

$$\frac{E_J}{k_BT} = \frac{hI_{c0}}{2ek_BT}\left[1-\sqrt{1-\frac{G_N}{4e^2/h}}\right] \qquad (8)$$

We fitted Eq. (8) to the data points with I_{c0} as the fitting parameter, and obtained reasonable agreement between experimental data (red squares) and calculation (blue line). The fitting yields I_{c0}=21 nA, 51% of the ideal value of ~ 41 nA. This reduction can be attributed (Beenakker 1992) to possible defects in Device 2. Thus, our data are well described by the phase diffusion model in the weak Josephson coupling regime.

In summary, we observe proximity effect induced superconductivity in S/SWNT/S Josephson junctions, in which the MAR processes and the supercurrent features can be tuned by the gate voltage. The finite zero bias resistance R_0 and magnitude of the switching current I_s in the *V*-*I* characteristics are in good agreement with the phase diffusion model in RCSJ.

Reference

Andreev, A. F. Sov. Phys. JETP 1964, 19, 1228.

Beenakker, C.W. J., *et al*., in Single Electron Tunneling and Mesoscopic Devices, edited by Koch, H., and Lubbig, H., (Springer, Berlin, 1992).

Beenakker, C. W. J. Three "universal" mesoscopic Josephson effects. In Transport Phenomena in Mesoscopic Systems, Fukuyama, H.; Ando, T., Eds. Springer: Berlin, 1992.

Bezryadin, A., *et al*., Nature (London) 2000, 404, 971.

Blonder, G. E., *et al*., Phys. Rev. B 1982, 25, 451.

Buitelaar, M. R., *et al*., Phys. Rev. Lett. 2002, 88, 156801.

Buitelaar, M. R., *et al*., Phys. Rev. Lett. 2003 91, 057005.

Buitelaar, M. R. *et al*., Phys. Rev. Lett. 2002, 89, 256801.

Chakravarty, S., *et al*., Phys. Rev. Lett. 1986, 56, 2303.

Cleuziou, J. P., *et al*., Nature Nanotech. 2006, 1, 53.

Cleuziou, J. P., *et al*., Phys. Rev. Lett. 2007, 99, 117001.

Eichler, A., *et al*., Phys. Rev. Lett. 2007, 99, 126602.

Fu, H. C., *et al*., Phys. Rev. Lett. 2006, 96, 157005.

Glazman, L. I., *et al*., Phys. Rev. Lett. 1997, 79, 3736.

Goswami, P., *et al*., Phys. Rev. B 2006, 73, 094516.

Goldman, A. M., *et al*., Phys. Today 1998, 51, No. 11, 39.

Herrero, C. P., *et al*., Phys. Rev. B 2002, 65, 104516.

Hoyos, J. A., *et al*., Phys. Rev. Lett. 2007, 99, 230601.

Ingold, G. L., *et al*., Phys. Rev. B 1994, 50, 395 402.

Jarillo-Herrero, P., *et al*., Nature (London) 2006, 439, 953.

Jorgensen, H. I., *et al*., Nano Lett. 2007, 7, 2441.

Jorgensen, H. I. *et al*., Phys. Rev. Lett. 2006, 96, 207003.

Joyez, P., et al., Phys. Rev. Lett. 1994, 72, 2458 2461.

Kasumov, A.Y., *et al*., Science 1999 284, 1508.

Kong, J., *et al*., Nature (London) 1998, 395, 878.

Lau, C. N., *et al*., Phys. Rev. Lett. 2001 87, 217003.

Lemay, S. G., *et al*., Nature 2001, 412, 617 620.

Liang, W. J., *et al*., Nature (London) 2001 411, 665.

Man, H. T., *et al*., Phys. Rev. B 2006, 73, 241401.

Martinis, J. M., *et al*., Phys. Rev. Lett. 1989, 63, 1507 1510.

Mason, N., *et al*., Phys. Rev. Lett. 1999, 82, 5341.

McKay, D., *et al*., Nature (London) 2008, 453, 76.

Morpurgo, A. F., *et al*., Science 1999, 286, 263.

Octavio, M., *et al*., Phys. Rev. B 1983, 27, 6739.

Penttila, J. S., *et al*., Phys. Rev. Lett. 1999, 82, 1004.

Refael, G., *et al*., Phys. Rev. B 2003, 68, 214515.

Rimberg, A. J., *et al*., Phys. Rev. Lett. 1997, 78, 2632.

Sahoo, S.; *et al*., Nat. Phys. 2005, 1, 99 102.

Tinkham, M., Introduction to Superconductivity (McGraw-Hill, New York, 1996).

Tsuneta, T., *et al*., Phys. Rev. Lett. 2007, 98, 087002.

Wilhelm, F. K., *et al*., Phys. Rev. Lett. 2001, 87, 136802.

Zhou, C., *et al*., Phys. Rev. Lett. 2000, 84, 5604.

Zhou, S. Y., *et al*., Nat. Phys. 2006, 2, 595 599.

Chapter V.

Fano Resonance on Carbon Nanotubes

V-1. Introduction

An emerging frontier in condensed matter research is the coherent, optics-like manipulation of electrons for information processing and storage. Recent advances in material sciences produced materials that can support phase coherent transport for hundreds and even thousands of nanometers, e.g. carbon nanotubes (Liang *et al*., 2001), graphene (Miao *et al*., 2007), and semiconductor heterostructures (Göres *et al*., 2000, Johnson *et al*., 2004). Interferometer, a staple of coherent optics, has been already realized in various systems. For instance, Fabry-Perot (Liang *et al*., 2001) and Sagnac (Bishara *et al*., 2008, Refael *et al*., 2007) interference were observed in high quality nanotubes, and Mach-Zehnder interferometer (Ji *et al*., 2003) has been realized using quantum Hall edge states.

In this chapter we report realization of an electronic double slit interferometer based on individual SWNT. Two SWNTs in close proximity are connected in parallel to metallic electrodes, but with significantly different transmission coefficients. As the Fermi levels of the electrodes are tuned through quantized energy levels, interference of transmission through these two channels give rise to a number of intriguing patterns in the conductance spectroscopy plots, including superposition of conductance oscillation with two different frequencies, charge sensing, Fano-like

line-shapes, inverse Coulomb blockade, and abrupt phase shifts. Our results demonstrate phase coherent transport in SWNT, which can be further exploited for optics-like manipulation of electrons.

V-2. Experiment Preparation and Differential *G* Spectroscopy

The device is fabricated on highly doped Si/SiO_2 substrates similarly as described in the chapter II. The electrodes consist of a thin adhesion layer of palladium and 70 nm of aluminum (Al). The silicon substrate serves as a back gate to modulate the carrier density in the SWNT (Fig. V-1a). Data presented in this chapter are taken from a device with source-drain separation of L=500±50 nm (the uncertainty arises from the finite extent of the electrodes' edges). At room temperature, the device resistance is ~ 10 kΩ, indicating highly transparent contacts between the nanotube and the electrodes. Although only one nanotube appears in atomic force microscope images, the room temperature saturation current is measured to be ~ 65 μA, suggesting that the device consists of either two SWNTs in parallel or one double-walled carbon nanotube.

We perform non-linear transport spectroscopy on the device, using standard lock-in techniques with a 5μV excitation voltage at 260mK in a ^{3}He refrigerator. Fig. V-2b plots the normal state differential conductance G_N at zero bias as a function of gate voltage V_g. Interestingly, $G_N(V_g)$ appears to be the superposition of two oscillations with different frequencies: the "background" conductance oscillates

sinusoidally with V_g, with relatively large period in gate voltage (~ 0.8 V), and a magnitude that varies between 70 to 160 μS; in contrast, the high frequency oscillation has saw-tooth line-shapes and a period of ~0.07 V in V_g.

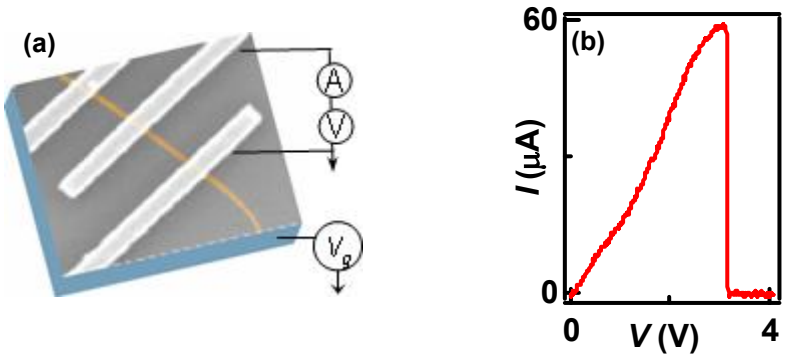

Fig. V-1. (a) schematics of the CNT device. (b) *I-V* curve of the CNT device, the device current saturates at around 60 μA.

Such conductance oscillation with two distinct frequency components has not been reported before. As shown in Fig. V-2a, which plots differential conductance as a function of V_g (horizontal axis) and source-drain voltage V (vertical axis), the 2-frequency conductance modulation persists through a large range in gate voltage and voltage biases. Here the anomalously large zero bias conductance peak, which appears as the white line at zero bias, arises from the superconducting proximity effect. Apart from the enhanced conductance at V<200μV, this proximity effect do not otherwise affect the transport characteristics, and will not be discussed further.

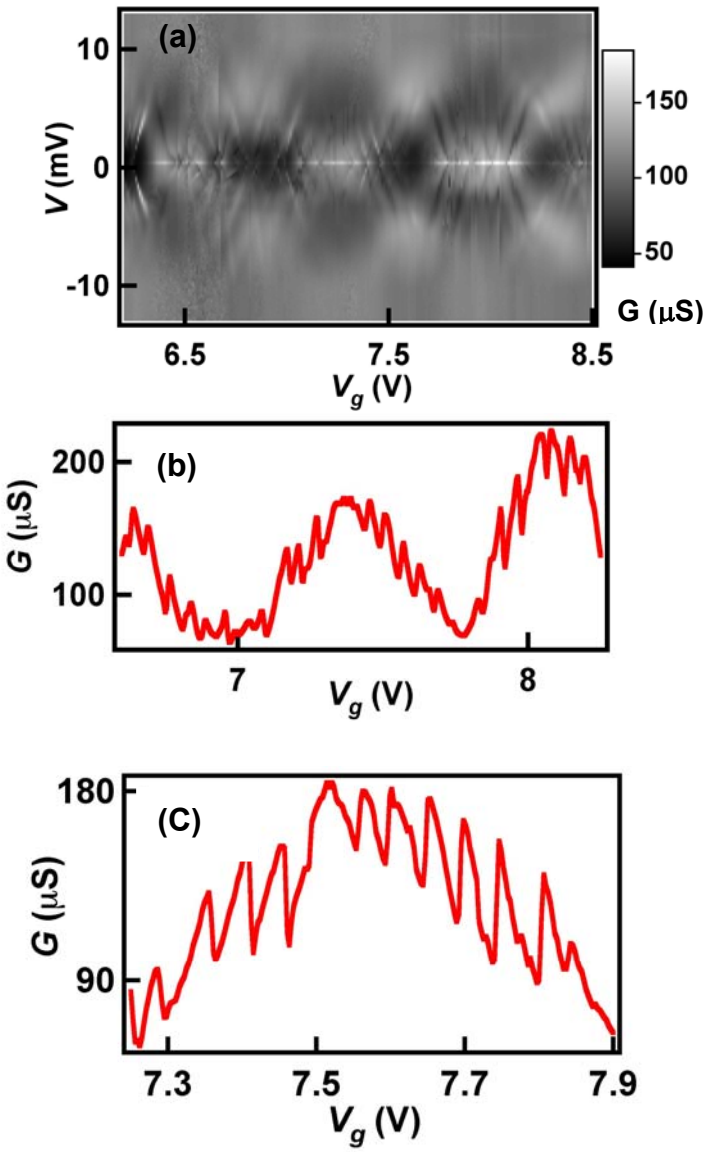

Fig. V-2. (a) differential conductance G vs bias V and gate voltages V_g. (b) Normal state conductance of the device as a function of V_g. (c) G vs V_g from 7.3V to 7.9V

V-3. Superimposition of Two Oscillations

In Fig. V-2a, the "slow" background oscillation forms the striking checker-board pattern, with alternating white and dark gray regions that correspond to high and low conductance, respectively. Such a checkerboard pattern is a signature of Fabry-Perot interference of incident and multiply-reflected electron waves within the nanotube.

The characteristic voltage scale, measured by the first conductance maximum value in bias in Fig. V-2a, is $V_c \approx 6$ mV. In the simple model of non-interacting electrons, the energy scale $eV_c = hv_F/2L$ corresponds to a 2π modulation in the phase accumulated by an electron in completing a roundtrip between two scatterers separated by distance L. Here $v_F \approx 10^6$m/s is the Fermi velocity of electrons in nanotubes. The value obtained from this estimate $L \approx 300$ nm is smaller than the source-drain separation, indicating the presence of impurities in the nanotube. Nevertheless, the regularity of the Fabry-Perot pattern suggests extremely low disorder (*e.g.* a single disorder located near the center of the nanotube device).

We now focus on the "fast" oscillations, which appear as sharp, dark lines that correspond to conductance dips. To examine them more closely, we perform high resolution spectroscopy of conductance vs V_g and bias. Fig. V-2c plots zero bias conductance $G(V_g)$ for the range $V_g = 7.3 - 7.9$V, spanning ~ 12 oscillation periods. We note that the sharp sawtooth oscillations display a phase change when the background conductance goes through the maximum, *i.e.* the curve changes from slow-rise followed by abrupt fall to abrupt-rise and slow decrease. These features strongly resemble those from charge sensing observed in GaAs/AlGaAs quantum dots (QD) (Johnson *et al*., 2004), in which the QD conductance of a quantum dot is sensitive to the changes in the number of electrons in a nearby island. For the GaAs/AlGaAs QDs, the electron number is typically controlled by a plunger gate that tunes the tunneling rate of electrons between the island and a reservoir. In our case,

since the device consists of two nanotubes, it is reasonable to assume that one of the nanotubes (NT-A) provides the background conductance with Fabry-Perot signatures, while the other tube (NT-B) acts as the island. When an electron jumps on the island, the effective gate voltage experienced by NT-A shifts by $-eV_g$, thereby abruptly shifting the $G_N(V_g)$ curve to the right. Thus, when the overall conductance is increasing (decreasing) function of V_g, the $G_N(V_g)$ curve exhibits a sharp drop (rise), as observed experimentally.

Despite the apparent agreement between our data and the picture of charge-sensing, transport characteristics of the device at finite bias reveals several unexpected features. Fig. V-3a and the top panel of 3b display high resolution non-linear transport spectroscopy $G_N(V_g, V)$ for two gate voltage ranges at magnetic B=0, each spanning several oscillation periods. The most striking features of these plots are the criss-crossing black lines that form a series of diamonds, with a characteristic size of ~ 2 mV. These diamonds are highly reminiscent those of Coulomb blockade(CB), which arises from resonant tunneling of single electrons across a quantized energy level in a quantum dot that is poorly coupled to the leads. However, there is one crucial difference between the standard CB patterns and our data: the former consists of a number of conductance *peaks* superimposed over a background with zero or very low conductance; our data, in contrast, consist of conductance *dips* on a high conductance background.

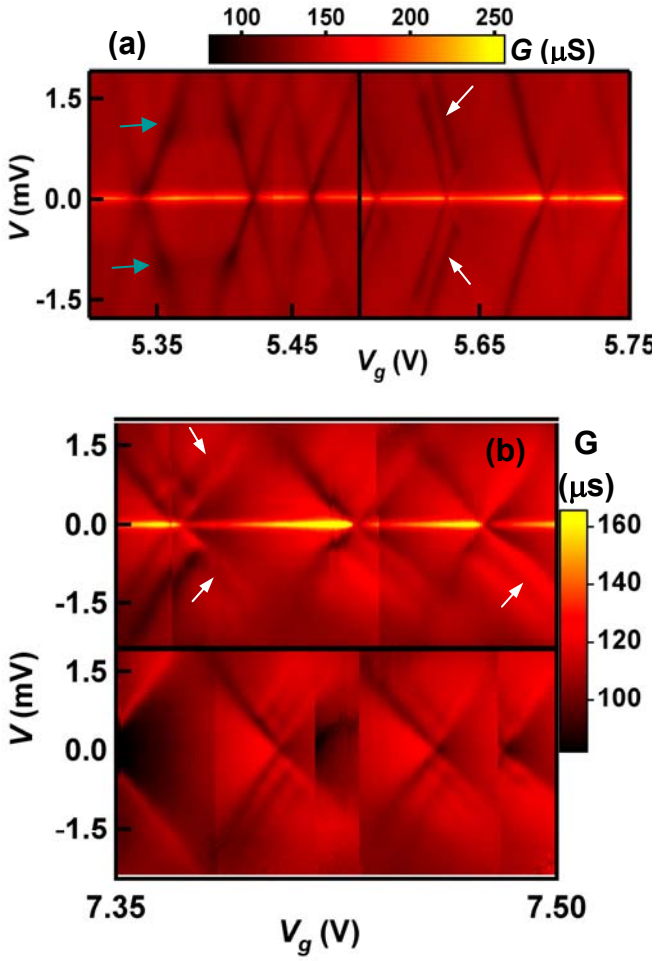

Fig. V-3. (a) High resolution G vs V and V_g in small scale, Blue arrows point at the co-tunneling G peaks, white arrows point at the excited energy levels tunneling, (b)Upper panel: high resolution G vs V and V_g from V_g =7.35V to 7.50V. Lower panel: G vs V and V_g at B=4T

V-4. Fano Resonance Interpretation and Simulation

Such "inverse Coulomb blockade" features have been observed in traditional QDs (Göres *et al*., 2000), and interpreted in terms of Fano resonance that arises from the interference of two conducting paths with different dwell times within the electron droplet. In our data the similarities between the data in Fig. V-3 and Coulomb blockade extend far beyond the diamond shape. For instance, in Fig. V-3a, two dark

horizontal bands at $V \approx 1$ mV appear within the diamond near V_g ~5.4V, indicated by the blue arrows, and strongly resemble features arising from inelastic co-tunneling in QD (Goldhaber-Gordon *et al*., 1998, Nygård *et al*., 2000, Kouwenhoven *et al*., 2001). More interestingly, there are several secondary lines parallel to, but separated by ~0.5 meV, from the main diamonds, as indicated by the white arrows in Fig. V-3a and V-3b. In high magnetic fields that are applied perpendicular to the nanotubes, these lines split into two. The splitting is roughly 0.26±0.2 meV at B=4T, as shown in the bottom panel of Fig. V-3b. Both the position and the field-induced splitting of the secondary lines are almost identical to those originating from electron tunneling through excited energy levels in QDs, which spin-split in large B (though these lines indicate dips in conductance rather than peaks). Thus we attribute the secondary lines to the excited levels in one of the nanotubes. We note that the observed magnitude of spin splitting yields an effective g-factor of 1.1, which is smaller than the value g=2 for free electrons. However, in an open QD, the g-factor may be reduced by, *e.g.* spin orbit coupling or exchange interaction with conduction electrons from the electrodes (Matveen *et al*., 2000, Brouwer *et al*., 2000). Thus, these "inverse" Coulomb blockade patterns, complete with features resembling Coulomb diamond, inelastic co-tunneling and excited energy levels, indicate that our data are far richer than simple charge sensing, which is not expected to be sensitive to the excited levels of the QD.

Here we sum our experimental observation thus far in this device that consist of two parallel carbon nanotubes, we have observed a rich set of patterns that are

indicative of a number of intriguing phenomena, including Fabry- Perot resonance, charge sensing, Fano resonance and "inverse" Coulomb blockade. We note that some aspects of these data have been observed previously. For instance, the inverse Coulomb blockade patterns have been observed in quantum dots fabricated on semiconductor heterostructures (Göres *et al*., 2000), and to a less extent, in SWNT (Aikawa *et al*, 2004, Yi *et al*., 2003). Individual sawtooth lineshapes in conductance (Fig. V-2b) resemble that of a Fano lineshape has also been reported in SWNT (Kim *et al*., 2003, Yi *et al*., 2004, Zhang *et al*., 2004). What sets our results apart is the clear superposition of two energy scales, the clarity of the resonant and excited energy levels, and the exceedingly large gate and bias ranges over which the patterns are observed. As such, the unprecedented observation of all 4 phenomena in one single data our data underscores the richness and uniqueness of our system and provide the best platform to date for understanding such phenomena.

The non-interacting Fano line shape is given by $g(E) = g_{inc} + g_{coh}\frac{|\varepsilon + q|^2}{\varepsilon^2 + 1}$, where g_{inc} and g_{coh} denote incoherent and coherent contribution to the conductance, $\varepsilon = 2(E - E_0)/\Gamma$ is the dimensionless detuning from the resonant level that has energy E_0, Γ is the level broadening due to the finite lifetime of electrons. The Fano parameter q determines the line shape as a peak ($q=\infty$) or a dip (q=0) or a dip followed by a peak (q>0) or a peak followed by a dip (q<0). Although most of analysis referring to the Fano effect is to find out the fitting parameter q, in our data

the Fano parameter q is not only indifferent value sand also in different signs. In Fig. V-2b, differential conductance and gate relation shows some dips followed by a peak and some peaks followed by a dip, indicating the Fano parameter changes sign if gate sweeps passing an extremum on the background conductance.

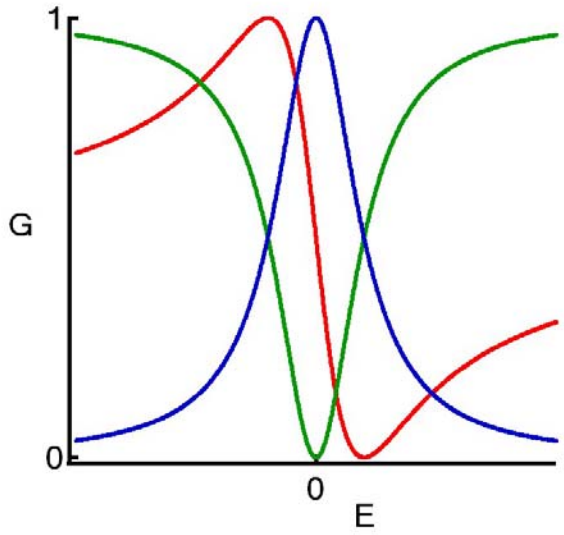

Fig. V-4. Renormalized Fano resonance lineshape with q=0 (green line), q=1 (red line) and q=1000 (blue line)

In the previous related reports (Kim *et al*., 2003, Yi *et al*., 2004, Zhang *et al*., 2004), these observations are explained in terms of Fano resonance, in which asymmetric lineshapes are generated as a result of interference between a continuum channel and a resonant channel. Here we propose a simple phenomenological model to account for our data: we assume two parallel conduction channels that interfere coherently. The first channel is NT-A that is well-coupled to the electrodes and gives rise to the Fabry Perot pattern, with a transmission amplitude given by $t_A = \sqrt{T_A} e^{i\phi}$,

where T_A is the channel's transmission coefficient and ϕ is the phase of the electron transmission. The second channel arises from NT-B that is poorly coupled to the electrodes, so that its transport is dominated by the Coulomb Blockade regime, with a transmission amplitude $t_B = \sqrt{T_B} i/(\varepsilon + i)$, where T_B is the transmission coefficient, $\varepsilon = 2(E - E_0)/\Gamma$ is the dimensionless detuning from the resonant level that has energy E_0, Γ is the level broadening due to the finite lifetime of electrons. These two channels coherently interfere to give rise to differential conductance $G=2e^2/h\ T_t$, with

$$T_t = \left|t_A + t_B\right|^2 = T_A + \frac{1}{1+\varepsilon^2}\left[T_B + 2\sqrt{T_A T_B}(\cos\phi + \varepsilon \sin\phi)\right]$$

Thus far this is similar to the standard analysis of Fano resonance (Babic *et al*., 2004). Crucially, however, the phase ϕ is no longer a constant, as assumed in the Fano resonance, but is energy-dependent, $\phi(E) = \frac{E}{h v_F} 2L + \phi_0$, where ϕ_0 is a constant. The total energy of the propagating electrons, E, in turn depends on both V and V_g, $E = \pm eV/2 - \alpha_{r,n} V_g$, where $\alpha_{r,n}$ is the gate coupling ratio for each channel, and the ± sign refers to alignment of the resonant level with the Fermi level in the source and drain electrodes, respectively. From Fig. V-2 and V-3, determines α is experimentally determined to be 0.03 for NT-A and 0.1 for NT-B, respectively. This is consistent with the expectation that a poorly coupled channel has higher α.

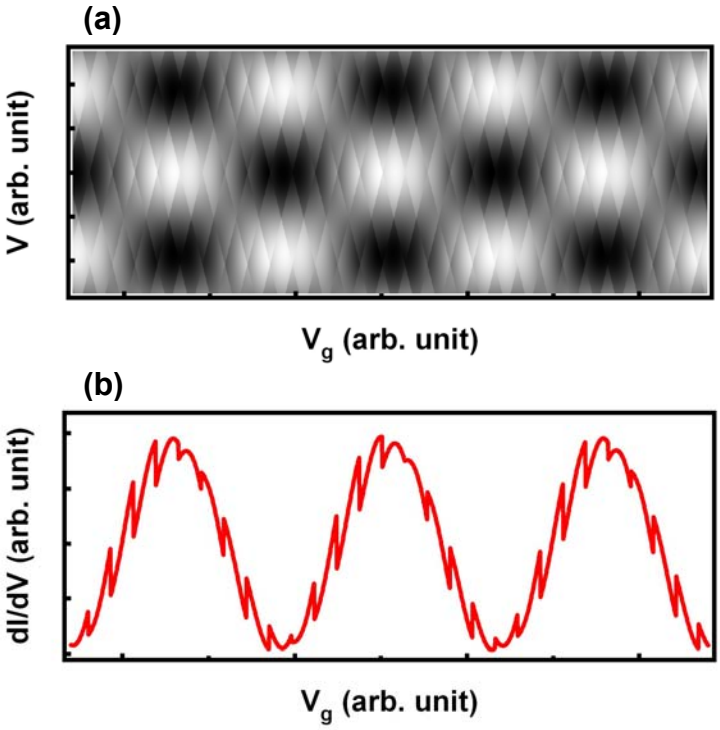

Fig. V-5. (a) Fano resonance simulation of G vs V and V_g, (b) simulation of G vs V_g at V=0V

We perform the simulation with the fixed transmission coefficient T_A=1.5 and T_B=0.5, and plot the simulated conductance spectroscopy in the large scale in Fig. V-5a, which represents superimposition of coulomb blockade diamond pattern and Fabry-Perot checker board pattern, indicating the simulation reproduces experimental data very well. Fig. V-5b is the G vs V_g line profile at zero bias from large scale simulation, showing a serious of dips on the background conductance, rather than simple peaks. Of particular importance is the line shape of the conductance dips in the differential conductance linear response. As shown in Fig. V-5b, the dips are asymmetric with slow rise followed by a sharp drop, as background conductance increasing; while the asymmetry is inversed, as background conductance decreasing.

Such abrupt shift of asymmetry parameter in the phase occurs whenever the background conductance passes through an extremum and repeats throughout the cycles. This feature is reproduced reasonably in our simulation.

Reference

Aikawa, H., *et al*, J. of Phys. Soc. Jpn., 2004, 73, 3235.

Babic, B., *et al*., Phys. Rev. B 2004, 70, 195408.

Bishara, W., *et al*., Phys. Rev. B 2008, 78, 165405.

Brouwer, P. W., *et al*., Phys. Rev. Lett. 2000, 85 , 369.

Fano, U., Phys. Rev. 1961, 124, 1866.

Refael, G., *et al*., Phys Rev Lett. 2007, 98, 24.

Goldhaber-Gordon, D., *et al*., Nature (London) 1998, 391, 156.

Göres, J., *et al*., Phys. Rev. B 2000, 62, 2188.

Ji, Y., *et al*., Nature 2003, 422, 415.

Johnson, A.C., *et al*., Phys Rev Lett. 2004, 93,106803.

Kim, J., *et al*., Phys. Rev. Lett. 2003, 90, 166403.

Kouwenhoven, L., *et al*., Phys. World 2001, Jan, 33.

Liang, W.J., *et al*., Nature 2001, 411, 665.

Matveev, K. A., *et al*., Phys Rev Lett. 2000, 85, 2789.

Miao, F., *et al*., Science 2007, 317, 1530.

Nygård, J., *et al*., Nature (London) 2000, 408, 342.

Yi, W., *et al*., Phys. Rev. Lett. 2004, 91, 076801.

Zhang, Z., *et al*., Europhysics Letters, 2004, 68(5), 713.

Chapter VI.

Fabrication of Grapheme *p-n-p* Junction with Contactless Gates

III-1. Fabrication of Suspended Structure

Transport in graphene *pnp* junctions is one of the most popular subjects in the graphene field. The most groups fabricate the local gates of graphene *pnp* junctions with an organic or a metal oxide layer as intermediate layer (Huard *et al*., 2007, Williams *et al*., 2007, Ozyilmaz *et al*., 2007, Oostinga *et al*., 2008), which may cause additional dopants or scattering sites.

We invented a multiple lithography technique to fabricate suspended structures, which can function as suspended top gates. The benefit of a suspended local gate is, the reduction of dopants or scattering sites and compatibility with the post annealing process. The height of the suspended structure can range 50 nm to a few micrometer, depending on the thickness of lift-off-resist (LOR). Its span can reach more than 12 micrometer with the help of a critical point drier (CPD). The whole fabrication only involves conventional e-beam lithography and e-beam evaporation with no etching, so the process is gentle, easy and well-controlled.

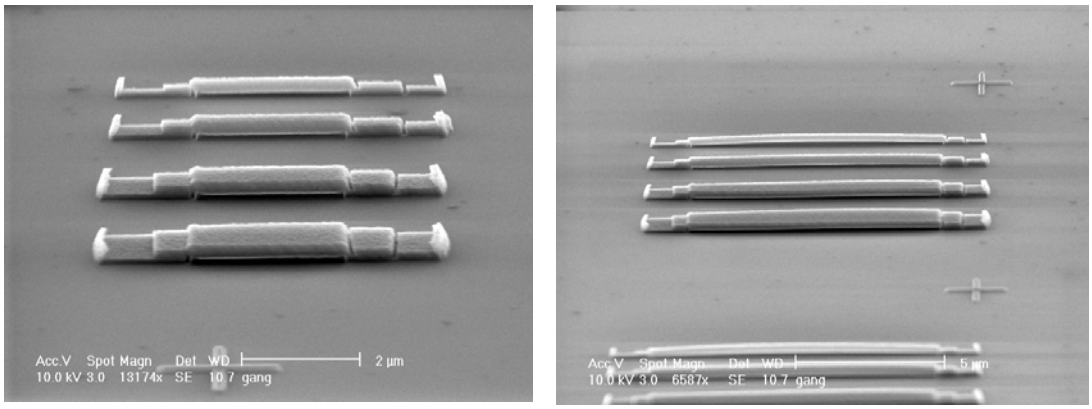

Fig. VI-1. 60^{o} side views of a few suspended Ti bridges, the scale bar is 2μm on left and 5μm on right

The main idea of our new technique is to develop bilayer resists separately with different developer. The bottom layer resist is LOR, which can be developed by MF319; and the top layer resist is PMMA, which can be developed by MIBK. Moreover, PMMA can be dissolved in acetone and PG remover, but LOR only in PG remover. Taking advantage of such different properties of two resists, we can make the suspended bridge with two steps of e-beam lithography and one step of e-beam evaporation.

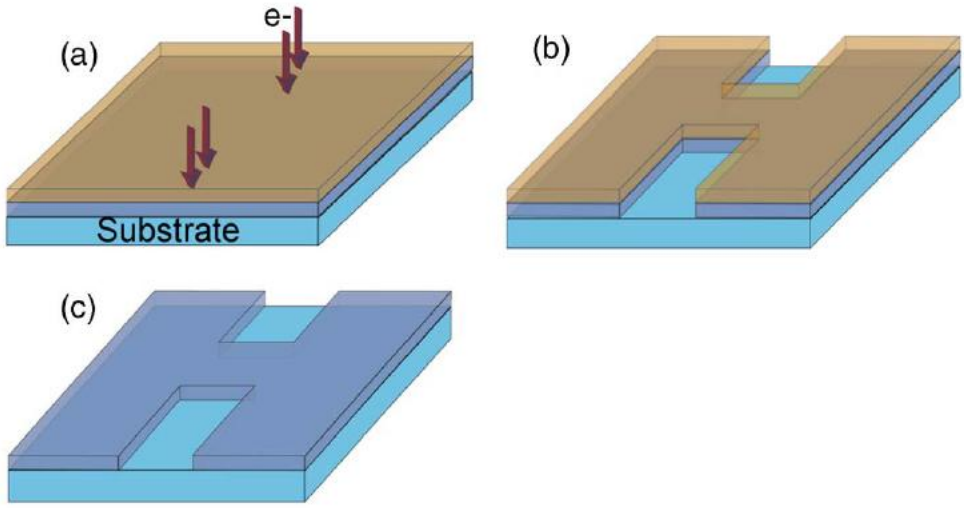

Fig. VI-2. schematics of fabrication process in the first EBL.

The goal of the first EBL is to create temporary support portion for the suspended bridge and windows for the electrical leads that contact the suspended bridge. As indicated in Fig. VI-2, LOR (dark blue) and PMMA (orange) are spun and baked separately on the wafer, which has predefined alignment marks. The spinning parameter of LOR 1A is the same as PMMA, and the baking parameter is 170°C and 5 minutes. Then e-beam exposes resists on two windows. Subsequently, the PMMA resist on these windows is developed by MIBK and rinsed by IPA and DI water, and then LOR is developed by MF319 in 25 seconds and rinsed by DI water. Finally, chip is dipped in acetone for 10 minutes and rinsed by DI water, and acetone dissolves the rest of PMMA and leaves LOR on the wafer. The final outcome of the first lithography step is a LOR layer with windows for electrical contacts for the air bridge.

In the second EBL, MMA (green) and PMMA (orange) are spun and baked on

top of LOR, as indicated in Fig. VI-3d. Then e-beam exposes a larger window including temporary support portion and electrical leads portion for the suspended bridge with the help of alignment marks. Then the bilayer resists are developed by MIBK and rinsed by IPA and DI water as usual. Finally, we have LOR as temporary support portion in the center, and open windows on each side for long term support and electrical contacts, and the rest of area is covered by three layers resist.

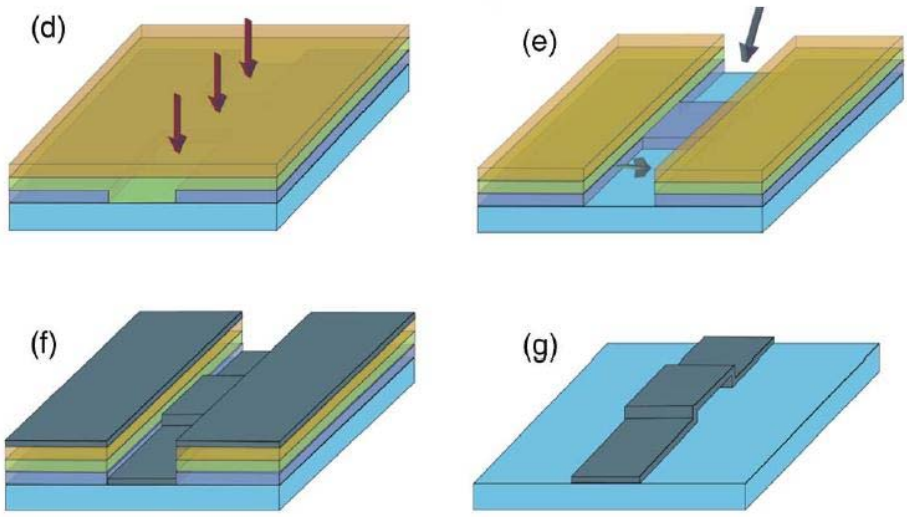

Fig. VI-3. schematics of fabrication process in the second EBL.

During the e-beam evaporation, the chip needs to be well-aligned well for deposition. 100 nm titanium is deposited from -45° and +45°, which ensures sufficiently thick vertical “walls” that support the suspended bridge. In the lift-off step, the LOR under the bridge and the rest of three layers resist are removed by PG remover, and the chip is gently blew dry by nitrogen gas or dried in CPD. Finally, the

suspended bridge as Fig. VI-3g is done. Maximum length of suspended bridge is 7 μm with nitrogen blow dry, while it can reach more than 12μm if a CPD is used.

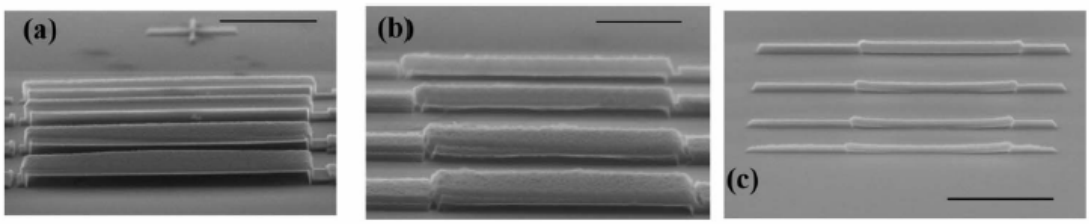

Fig. VI-4. three SEM images of a few suspended bridges, scale bar is 2μm.

By controlling the pattern of EBL, we can tune the length and width of suspended bridges. Fig. VI-4a shows fours suspended bridges with 100nm, 150nm, 200nm, 250nm width, and their height above the substrate is 300nm. The bridges in Fig. VI-4b and c are 100nm high and 50nm high respectively. These images suggest that shorter and wider bridges are more robust. The height is determined by the type of LOR, for example, LOR 1A is about 100nm thick and its suspended bridge is 100nm too. So we could choose different commercial LOR, such as LOR 3A, 1A and 0.5A, or dilute the LOR with solvent to control the thickness of LOR and height of suspended bridges.

III-2. Fabrication of Grapheme *p-n-p* Junction with Suspended Gates

With the new technique of suspended structure, the bridge can be fabricated across the graphene and behaves as a local gate to tune the type and the number of

carriers on the covered graphene portion. The back gate control the rest of graphene, so a graphene *p-n-p* device can be created. A few groups have reported grapheme *p-n-p* junction investigation (Huard *et al*., 2007, Williams *et al*., 2007, Ozyilmaz *et al*., 2007), and most of their device applied intermediate materials between graphene and local top gate, such as HfO, Al_2O_3. We are the first group reporting grapheme *p-n-p* junction with suspended gates, which have three advantages. First, the vacuum insulated gap between the bridge and device is a robust dielectric that, compared to the conventional dielectrics, is less susceptible to pinholes and leakage current, and minimizes the damage to the atomic layer. Second, the fabrication of suspended top gates is simple and gentle. Unlike other techniques to fabricate suspended structures, our technique protects graphene from any damage in those depositions or removing process. Third, it is also compatible with post-fabrication annealing, which improves device mobility by removing resists residual and adsorbate on the graphene surface.

I now describe the general fabrication procedure for grapheme *p-n-p* junctions with suspended gates. In general, we fabricate the top gate first and contact leads later, to avoid oxidation of the contact layer, which would increase contact resistance. Before either step, however, at least two groups of new alignment marks need to be made closed to the flake. One is used for two EBL of top gate fabrication, and the other is used for contact leads fabrication. During the pattern design, different parts of the pattern including the top gates, contact leads and new alignment marks, need to be designed together, and then separated into different DC2 file.

The first step is to fabricate the new alignment marks with an EBL and a deposition, And second step fabricates the top gate across the graphene sheet as described above. The third step fabricates the contact leads by general EBL with MMA/PMMA and deposition with Ti /Au (5nm/80nm). Before the third step, oxygen cleaning is necessary to remove the resist residue. The cleaning is done in the furnace at 300°C for 30 minutes with 0.4 SLM of oxygen flow. If the CPD is used in the second step, it would also be necessary at the end of third step. After completion of fabrication, the device needs to be annealed thermally via a local heater in the high vacuum. Local heater annealing eliminates impurities on the graphene, moves Dirac point back to zero gate voltage and improve device mobility. Typically the annealing should be performed immediately before the cool down, and transferred quickly from annealing stage to measurement insert, otherwise the device may be contaminated by the air again.

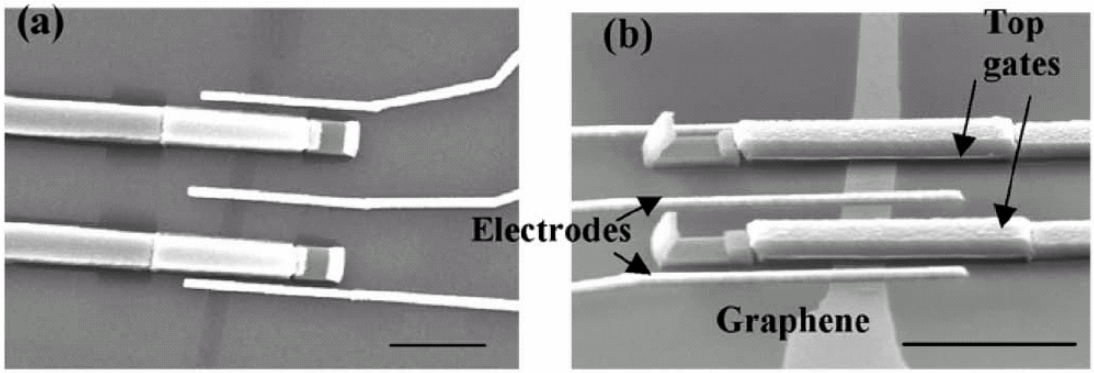

Fig. VI-5. Two SEM images of graphene *p-n-p* junction devices, scale bar is 2μm. (a), a devices top view. (b), a 60^{o} side view

Reference

Huard, B., *et al*., Phys. Rev. Lett. 2007, 98, 236803

Oostinga, J.B., *et al*., Nature Mater. 2008, 7, 151.

Ozyilmaz, B. *et al*., Phys. Rev. Lett. 2007, 99, 166804.

Son, Y. W., *et al*., Phys. Rev. Lett. 2006, 97, 216803.

Williams, J. R., *et al*., Science 2007, 317, 638.

Chapter VII.

Transport in Grapheme *p-n-p* Junction with Contactless Gates

VII-1. Introduction to Graphene *p-n-p* Junction

A remarkable electronic property of graphene is that both its carrier type and density can be electrostatically controlled. With local top gate and global back gate, different segments of graphene can be controlled separately and form *p-n* junctions (Huard *et al*., 2007, Williams *et al*., 2007, Ozyilmaz *et al*., 2007, Oostinga *et al*., 2008, Fogler *et al*., 2008, Abanin *et al*., 2007, Gorbachev *et al*., 2008), which have been demonstrated or predicted to give rise to quantum Hall plateaus with fractional values (Williams *et al*., 2007, Ozyilmaz *et al*., 2007, 2008, Abanin *et al*., 2007), Veselago lensing (Cheianov *et al*., 2007, Cserti *et al*., 2007) and Klein tunneling (Katsnelson *et al*., 2006, Cheianov *et al*., 2006). A few groups have observed fractional quantum Hall plateaus in the graphene *p-n-p* junction, but most of the experiments apply an organic or a metal oxide layer as intermediate layer, which may cause additional dopants or scattering sites. Our new technique as described in the previous chapter, allows us to fabricate grapheme *p-n-p* junction with contactless gates and hence minimal damage to the atomic layer. We observe fractional quantum Hall plateaus in the differential conductance spectroscopy, and the presence of the $2e^2/h$ conductance plateau at high magnetic fields demonstrates the quality of our graphene *p-n-p* junction.

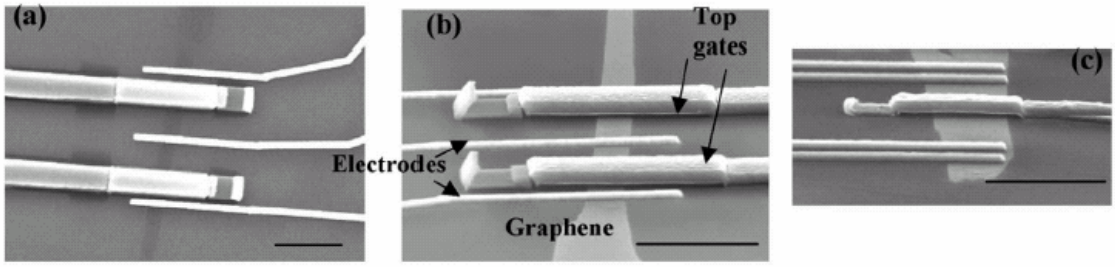

Fig. VII-1. SEM images of graphene *p-n-p* junction with a contactless gate

VII-2. Transport Measurement in Graphene *p-n-p* Junction

The devices discussed in this chapter are fabricated on the highly doped Si wafer with 300nm SiO_2 top layer, and the air gap between top gate and graphene is 100nm. All of the measurements are performed in the He3 pumped cryostat at temperature of 260mK.

The device's differential resistance R is plotted in Fig. VII-2a as functions of the back gate voltage V_{bg} (vertical axis) and top gate voltage V_{tg} (horizontal axis). The most visible feature is the horizontal red band at V_{bg} ~14 V corresponding to Dirac point on the uncovered region of graphene, the diagonal white narrow band corresponding to Dirac point on the top gate covered region of graphene. The cross point of four regions is where the entire graphene is tuned at Dirac point. Two bands divide the plot into four different regions corresponding to the different doping status in each graphene section, as indicated in the figure. For example, on the left upper region, the uncovered graphene section is electron doped by the controlled of global back gate, and top gate covered section is hole doped by the controlled of back and

top gate, so the entire graphene between the source and drain electrodes is tuned as a *n-p-n* junction. The presence of two Dirac points is more easily seen in Fig. VII-2b, which plots R versus V_{bg} at three different top gate values. From the red curve, the mobility of the device is estimated to be 8500 cm^2/Vs. On the side of center peak, the orange curve and blue curves have additional shoulders at V_{bg} ~-14V and 28V, corresponding to Dirac point of the top gate covered section. We observe additional shoulders instead of well-developed peaks, because the top gate only covers less 15% area of the entire junction. Our results clearly demonstrate individual control of separate regions in the graphene device.

The ratio of the coupling efficiencies η of back gate and top gate to graphene can be estimated by the slope of white band which is 1.27. η is typically given by the capacitance between gate and graphene per unit area, $C=\varepsilon\varepsilon_0/d$, where ε_0 is the permittivity of free space, d is the separation between the gate and graphene, ε is the dielectric constant of the material between gate and graphene, which is 3.9 (SiO_2) for back gate and 1 (vacuum) for the top gate. So the coupling ratio is, $\frac{C_{bg}}{C_{tg}}=\frac{\varepsilon_{bg}}{\varepsilon_{tg}}\frac{d_{tg}}{d_{bg}}\approx$ (3.9)(100/300)≈1.3, in excellent agreement with the data.

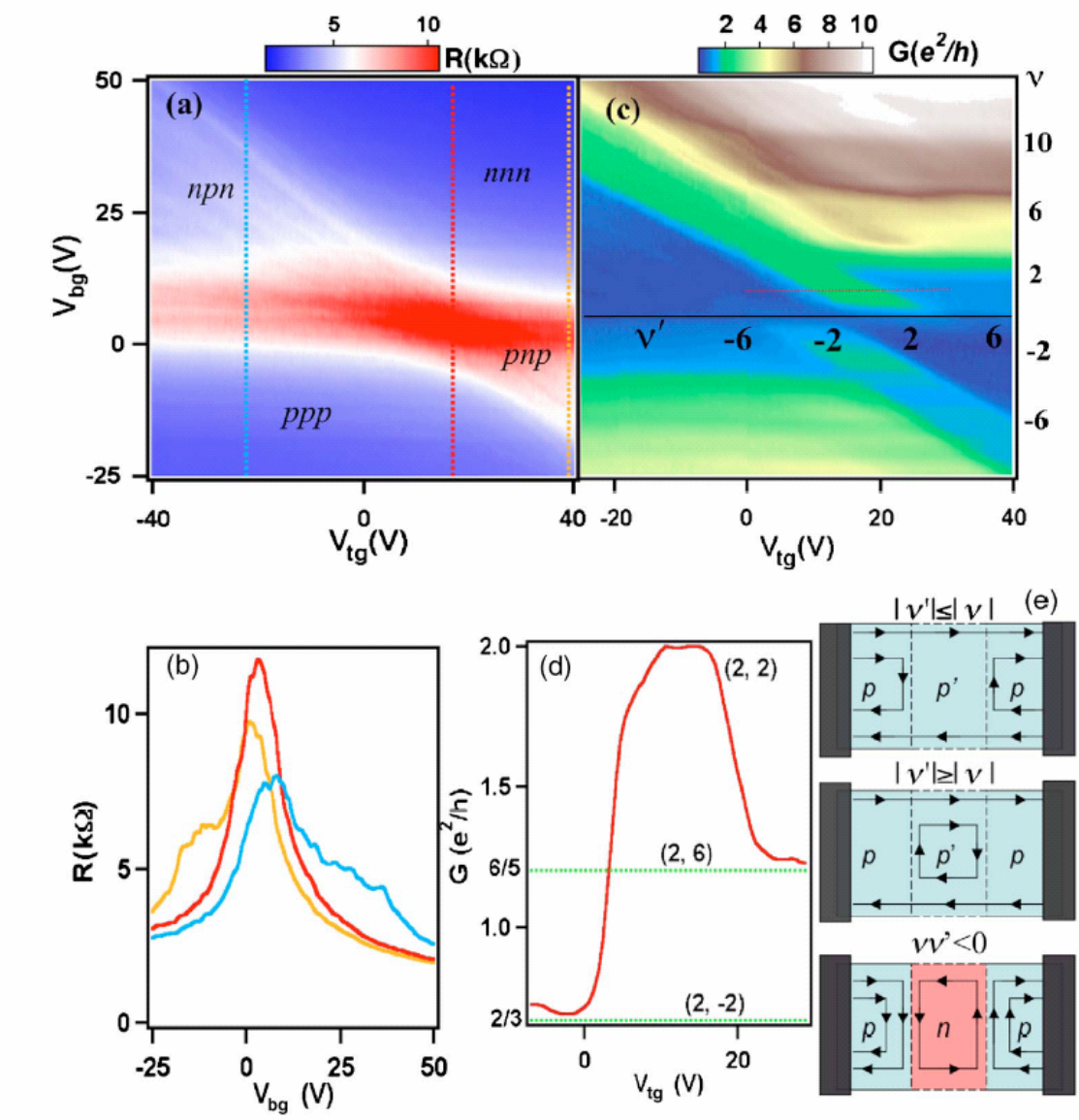

Fig. VII-2. (a), Differential resistance of a graphene device with a center top gate covering 15% of the device area as functions of V_{bg} and V_{tg}. The dotted lines correspond to the line traces in (b). Doping combinations for different regions are labeled. (b) Differential resistance as a function of V_{bg} at different V_{tg}. (c). Device conductance at 8 T magnetic field as functions of V_{bg} and V_{tg}. For reference, the filling factors ν and ν' are also labeled (d). Line trace along the red line in (c). The bracketed numbers correspond to (ν, ν') for the plateaus. (e). Schematics of edge state propagation for different values of (ν, ν').

Further evidence for the formation of graphene *p-n-p* junctions is provided by

transport data at magnetic field of 8 T. In the high magnetic field, differential conductance of a graphene device with uniform carrier density quantize at a series of conductance plateaus at half integer values of $4e^2/h$, due to the formation the quantum Hall edge state. In graphene *p-n-p* junctions, we observed fractional quantum Hall plateaus as indicated in Fig. VII-2c. Filling factors ν and ν' corresponding to uncovered and covered sections are labeled at both axes. They are related to the gate voltages by $n_c h/eB$, where h is the Planck's constant, e is the electron charge, and n_c is the charge density, given by $C_{bg}V_{bg}/e$ in the uncovered section, and $(C_{bg}V_{bg}+C_{tg}V_{tg})/e$ in the covered section. Fig. VII-2d is a G vs V_{bg} curve taken at V_{bg} =10 V, which clearly presents the plateaus at 2/3, 2 and 6/5. Our results are very similar to those reported by Dr. Kim (Ozyilmaz *et al*., 2007), and confirm the presence of two *p-n* interfaces.

The two terminal conductance of homogeneous graphene in the high magnetic field quantizes at the value $G=\nu e^2/h$, where the value of filling factor could be 2, 6, 10, as indicated on the axis of Fig. VII-2c. In the graphene *p-n-p* junctions, the fractional plateaus values arise from the partial and full equilibration of the edge states at the *p-n* interface, depending on the signs and magnitude of ν and ν'.

When the polarities of two sections are the same, and the carrier density in the uncovered section is larger than in the covered section $\left(|\nu| \geq |\nu'|\right)$, the number of modes in the uncovered section is more than that in covered section as first case indicated by the upper panel in Fig. VII-2e. Then net conductance is given by

$$G = \frac{e^2}{h}|\nu'| = 2\frac{e^2}{h}, 6\frac{e^2}{h}, \ldots \qquad (|\nu| \geq |\nu'|)$$

When the polarities of two sections are the same, and the carrier density in the uncovered section is smaller than in the covered section $(|\nu| \leq |\nu'|)$, the number of modes in the uncovered section is less than covered section, as indicated by the middle panel in Fig. VII-2e. The conductance is differently given by

$$G = \frac{e^2}{h}\frac{|\nu||\nu'|}{2|\nu'| - |\nu|} = \frac{6}{5}\frac{e^2}{h}, \frac{10}{9}\frac{e^2}{h}, \ldots \qquad (|\nu| \leq |\nu'|)$$

In both of above cases, the entire device is at status of *n-n-n* or *p-p -p* junctions.

When the polarities of two sections are different $(\nu\nu' \leq 0)$ as shown by the lower panel in Fig. VII-2e, the modes of edge states in each section are full equilibration at the *p-n* interface. Then the conductance is obtained as

$$G = \frac{e^2}{h}\frac{|\nu||\nu'|}{2|\nu'| + |\nu|} = \frac{2}{3}\frac{e^2}{h}, \frac{5}{6}\frac{e^2}{h}, \ldots \qquad (\nu\nu' \leq 0)$$

In this case, the device is in the status of *n-p-n* or *p-n -p* junctions.

In Fig. VII-2d, the conductance filling factor is tuned by the V_{tg} from 2/3, 2 to 6/5, which passes through *n-p-n* junctions to *n-n-n* $(|\nu| \geq |\nu'|)$ $(|\nu| \leq |\nu'|)$ junction. The experimental value is in great agreement with theoretical value. In particular, we note that the conductance plateau with the full value of $2e^2/h$ was not observed in Kim's paper (Ozyilmaz *et al*., 2007), due to the strong effect of backscattering on states with $|\nu| = |\nu'|$. In contrast, the plateau at $2e^2/h$ is well developed as shown in Fig. VII-2d, establishing that transport in our *p-n-p* junctions experiences relatively

weak backscattering.

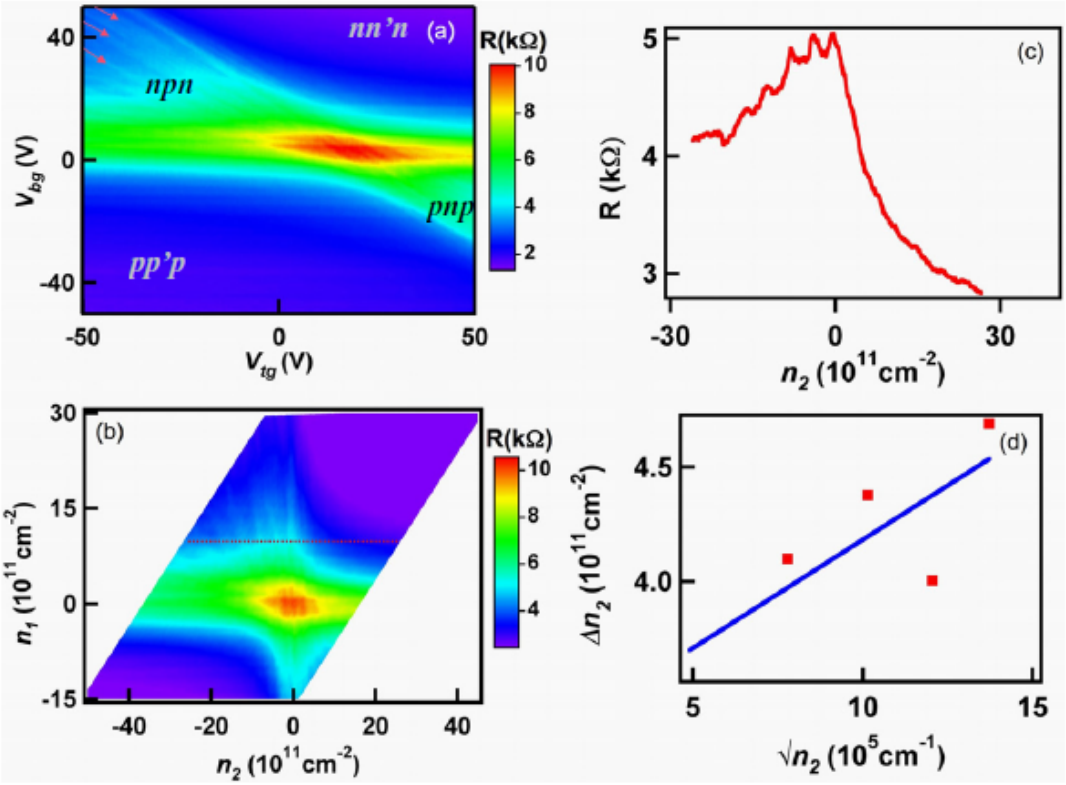

Fig. VII-3. *pnp* junction data in zero magnetic field. (a) Four-terminal device resistance as functions of V_{bg} and V_{tg}. The arrows indicate oscillations in the *npn* region. (b) Same data as (a), but plotted against n_2 and n_1. (c) Line trace along the dotted line in (b), showing resistance oscillation as a function of n_2. (d) The peak spacing Δn_2 vs $\sqrt{n_2}$. The line represents a linear fit to the data.

We now focus exclusively on the upper left region of Fig. VII-3, i.e. where the junction is in the *npn* regime. Compared with the neighboring unipolar (*pp'p* or *nn'n*) regions, the junction resistance is significantly higher, as expected at the boundary of a *pn* junction. More interestingly, we observe resistance oscillations as a function of

both V_{bg} and V_{tg}, as indicated by the arrows in Fig. VII-3(a). Notably, these oscillations are not found in the unipolar regions. Such oscillations were first reported by Young and Kim (Young *et al*., 2009), and arise from Fabry–Perot interference of the charges between the two p–n interfaces. Thus, the holes in the top-gated region are multiply reflected between the two interfaces, interfering to give rise to standing waves, similar to those observed in carbon nanotubes (Liang *et al*., 2001) or standard graphene devices(Miao *et al*., 2007). Modulations in n_2 change the Fermi wavelength of the charge carriers, hence altering the interference patterns and giving rise to the resistance oscillations.

To analyze these oscillations in detail, we re-plot the data in Fig. VII-3(a) in terms of n_2 and n_1. Assuming in a parallel plate geometry between the gate and the device, $C_{bg}/e \approx 7.19\times10^{10} cm^{-2}$. However, from quantum Hall measurements, we estimate the effective capacitance to be $\sim C_{bg}/e \approx 6.51\times10^{10} cm^{-2}$. This small discrepancy may be attributed to a slightly thicker SiO_2 layer, slightly smaller ε_{bg}, or additional screening by the electrodes. Using this value, we have $n_1 = 6.5\times10^{10}(C_{bg} - C_{D,bg})cm^{-2}$ and $n_2 = 6.5\times10^{10}[(C_{bg} - C_{D,bg}) + \eta(C_{tg} - C_{D,tg})]cm^{-2}$. The new plot is shown in Fig. VII-3(b). The color scale is adjusted to accentuate the resistance oscillations, which appear as fringes fanning out from the Dirac point at n_1=n_2=0. Fig. VII-3(c) shows the device resistance versus n_2 at $n1 = 1.3\times10^{12}$ cm^{12}, displaying clear oscillations.

Within the Fabry–Perot model, the resistance peaks correspond to minima in the

overall transmission coefficient; the peak separation can be approximated by the condition $k_F(2L) = 2\pi$, i.e. a charge accumulates a phase shift of 2π after completing a roundtrip 2*L*c in the cavity. Here k_F is the Fermi wave vector of the charges, and *L*c is the length of the Fabry–Perot cavity. Under the top gate, $k_{F2} = \sqrt{\pi n_2}$, so the spacing between successive peaks is estimated to be $\Delta n_2 = 4\sqrt{\pi n_2} / L_c$. In Fig. VII-3(d), we plot the measured peak spacing for the curve shown in Fig. VII-3(c) against $\sqrt{n_2}$. The data points fall approximately on a straight line. The best linear fit yields a line with a slope 0.95×10^5 cm^{-1}, corresponding to *L*c = 740 nm. This agrees with the value estimated from electrostatics, *L*c= L_{tg} + 2*d*, as the electric field induced by the top gate on the device is expected to extend by a distance ~*d* away from either edge. Finally, we note that the device in (Young *et al*., 2009) had extremely narrow gates L_{tg} < 20 nm. In comparison, our top gate spans a much larger distance, L_{tg} ~500 nm. Thus, the observation of clear Fabry–Perot interference patterns underscores the high quality of our *pnp* graphene devices.

Reference

Abanin, D. A., *et al*., Science 2007, 317, 641.

Berger, C., *et al*., Science 2006, 312, 1191.

Bolotin, K. I., *et al*., Solid State Comm. 2008, 146, 351–355.

Chen, Z. H., *et al*., Physica E (Amsterdam) 2007, 40, 228.

Cheianov, V. V., *et al*., Science 2007, 315, 1252.

Cheianov, V. V., *et al*., Phys. Rev. B 2006, 74, 041403(R).

Cserti, J., Phys. *et al*., Rev. Lett. 2007, 99, 246801.

Du, X., *et al*., Nat. Nanotechnol. 2008, 3, 491–495.21.

Fogler, M. M., *et al*., Phys. Rev. B 2008, 77, 075420.

Gorbachev, R. V., *et al*., Nano Lett. 2008, 8, 1995.

Han, M. Y., *et al*., Phys. Rev. Lett. 2007, 98, 206805.

Huard, B., *et al*., Phys. Rev. Lett. 2007, 98, 236803.

Katsnelson, M. I., *et al*., Nat. Phys. 2006, 2, 620.

Liang, W.J., *et al*., Nature 2001, 411 665–9.

Miao, F., *et al*., Science 2007, 317, 1530.

Moser, J., *et al*., Appl. Phys. Lett. 2007, 91, 163513.

Nikolaos, T., *et al*., Nature (London) 2007, 448, 571.

Novikov, D. S., *et al*., Phys. Rev. Lett. 2007, 99, 056802.

Novoselov, K. S., *et al*., Nature (London) 2005, 438, 197.

Novoselov, K. S., *et al*., Science 2004, 306, 666.

Oostinga, J.B., *et al*., Nature Mater. 2008, 7, 151.

Ozyilmaz, B. *et al*., Phys. Rev. Lett. 2007, 99, 166804.

Williams, J. R., *et al*., Science 2007, 317, 638.

Young, A., *et al*., Nat. Phys. 2009, 5 222–6.

Chapter VIII.

Electronic Transport in the Normal Metal – Graphene – Superconductor Junctions

VIII-1. Instruction

Recently several groups reported the study on the graphene based JJ systems (Heersche *et al*., 2007, Du *et al*., 2008, Miao *et al*., 2007, Lutchyn *et al*., 2008, Titov *et al*., 2006), in which phenomena such as gate tunable supercurrent, none-zero supercurrent the Dirac point, multiple Andreev reflections, have been experimentally observed. Due to the unusual nature of Dirac fermion on graphene, specular Andreev reflection at the graphene - superconductor interface is predicted by several theoretical works (Beenakker 2006, Cheng *et al*., 2009). An Andreev reflection (AR) is electron – hole conversion at a superconductor-normal metal interface (Andreev 1964). AR gives rise to the doubling of the conductance of a metal in the ballistic regime. When the reflected hole retraces the path of the incident electrons, the process is called retro-AR, which is the usual process at a superconductor-normal metal interface. By comparison, the reflected hole can also be specularly reflected, as shown in Fig. VIII-8b, which has never been observed experimentally. Graphene offers a good two dimensional system to study specular Andreev reflection, which is an essentially two dimensional effect. To this end, we studied the electronic transport in the normal metal – graphene – superconductor Junctions (NS junctions), and observed

differential conductance peaks at superconducting energy gap. No specular AR has been observed; further studies with higher mobility of the device will be necessary.

VIII-2. Device Fabrication

Graphene preparation is the same as the previous chapter. The difficulty presented by this project is the fabrication of high quality graphene devices with different material electrodes. We have tried three different fabrication methods, which are angle evaporation, shadow mask and two steps EBL. The data present in the following sections are mostly from the latter method.

The angle evaporation method involves only one step of EBL and two steps of angle evaporation. After graphene preparation on the substrate, we expose bilayer resists and open windows as the red opening shown in Fig. VIII-1(a). The developing time is increased to 65~70 s, so that the undercut in MMA is larger for convenience of the angle evaporation. Then angle evaporations from the left and right with 45^0 angles are performed. In this process, the sample is attached to a 45^0 angle sample holder. Generally 10 nm Ti and 50 nm Au are evaporated first, and then we vent the chamber and flip the holder, followed by evaporating 5 nm Ti and 80 nm Al. After these steps of evaporation, graphene is covered by two electrodes with different materials, which are connected to the bonding pad with different connections.

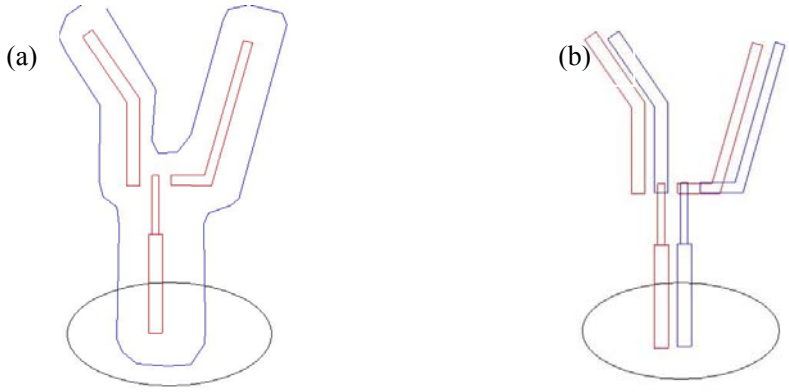

Fig. VIII-1. (a) schematics of EBL pattern: red windows are opened by EBL, blue window is the MMA undercut, and black circle represents the graphene flake (b) device geometry after two steps angle evaporation: red color represents normal metal, and blue color represents superconducting metal.

The advantage of angle evaporation is the reduction in the fabrication steps, and we expect high quality from devices due to the single lithography step. However, for reasons not understood the device's conductance dependence on gate is very poor, and the mobility is very low. The potential reason is that the current passes too many metals interface between bonding pad and graphene. For instance, the right electrode in Fig. VIII-1(b) is connected to the bonding pad through a route of graphene (black) – superconducting electrode (blue) – normal metal connection (red) - superconducting connection (blue), resulting in device's conductance dominated by the electrode's conductance. Therefore, we move to another method.

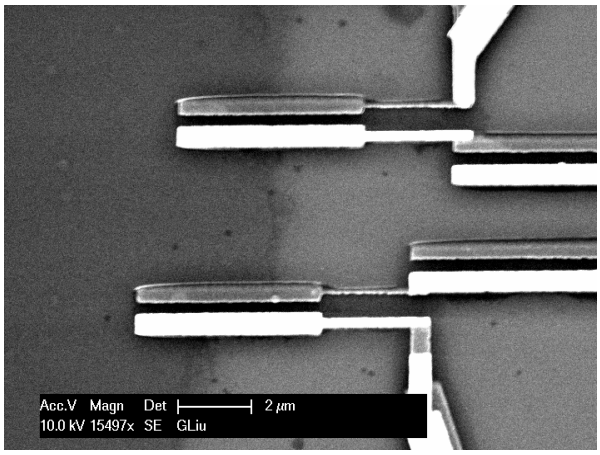

Fig. VIII-2. SEM image of a device by angle evaporation method

Secondly, we try the shadow mask method. With Wenzhong Bao's help, we design and fabricate the shadow mask as described in the reference (Bao *et al*., 2010). Then we just need to align the shadow mask with graphene flake and do two evaporations. The NS devices fabricated by shadow mask have the smallest contact resistance, because the process of fabrication does not involve any EBL or any resist residue. The figures in Fig. VIII-3 are the SEM images of NS junctions devices made by shadow mask. However, the alignment process is performed using the micro position aligner under the optical microscope, so the resolution of the alignment is limited to 0.5~1μm.Thus, the device separation can not be reduced to be under 500nm, practically limiting device to the diffusive regime. Therefore we have to look for an alternate fabrication method.

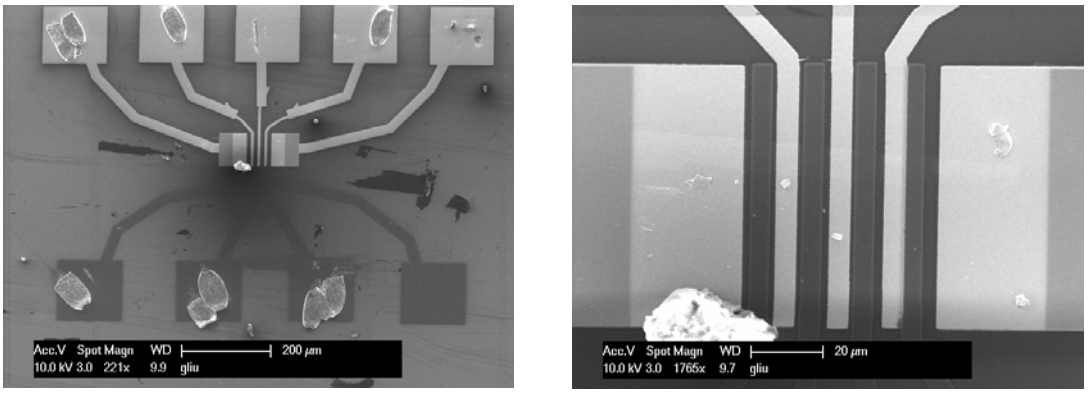

Fig. VIII-3. two SEM images of NS devices by shadow mask method

Our last technique involves separate fabrication of the electrodes. One EBL and evaporation are performed for fabrication of the normal metal electrode, and a second EBL and evaporation for the superconducting metal. The challenge of the two EBL steps is that the normal metal and graphene interface could be deteriorated during the second EBL. This is indicated by the fact that normal metal electrode contact is much larger than superconducting metal electrode contact. We believe that Ti sticking layer of normal metal electrode is oxidized when the second EBL resists are baked at 170^0C. So to protect the normal metal contact, we perform the second EBL resists baking in the Rapid Thermal Annealer with nitrogen gas (as opposed to on the hot plate in the air) This modification significantly increases our device yield with 2 transparent contacts. Another benefit of this method is that the electrode separation is well controlled by the pattern design, and can easily be as small as 100~200 nm. Finally, after the device fabrication, devices are annealed in the vacuum with local heater for

improving the device mobility. The data presented in the following sections is obtained from the devices fabricated by this method.

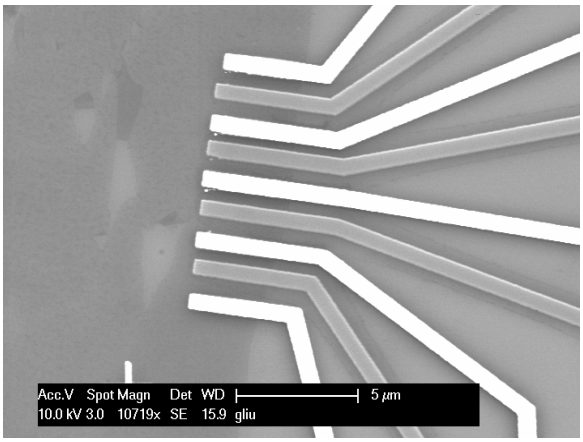

Fig. VIII-4. SEM image of NS devices by two EBLs method. The dark electrodes are normal metal (Ti/Au), and the light electrodes are superconducting metal (Ti/Al).

VIII-3. Differential *G* Spectroscopy

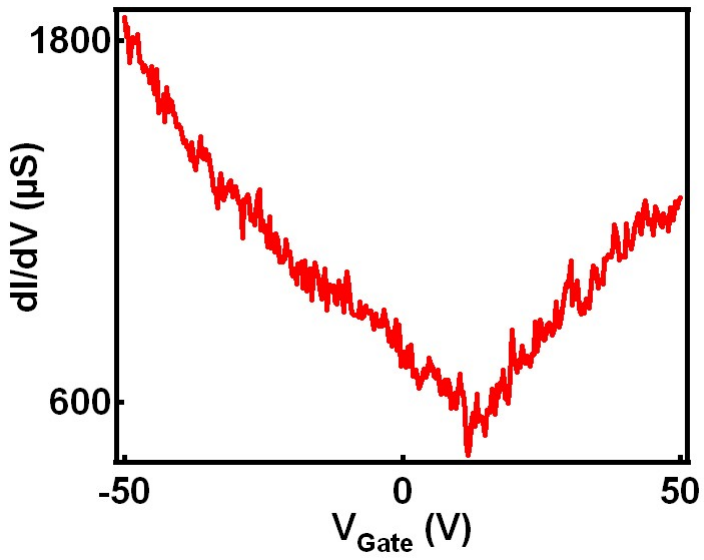

Fig. VIII-5. Differential conductance as a function of back gate voltage

We perform non-linear transport spectroscopy on the device, using standard lock-in techniques with a 5μV excitation voltage at 260mK in a ^{3}He refrigerator. The mobility of the device is around 1000 cm^2/Vs estimated from differential conductance response to gate in Fig. VIII-5, and Dirac point of the device is located at V_g=11.2 V. Fig. VIII-6 plots the differential conductance as a function of bias voltage and gate voltage. As expected, as the gate voltage is varied, the conductance of the device reaches the minimum value at Dirac point V_g=11.2 V, and increases as the gate voltage sweeps away from Dirac point. On the dimension of bias voltage, two conductance peaks are observed at V_{bias} =±140μV as shown by the arrows on Fig. VIII-6. The differential conductance as a function of bias voltage are plot at highly doped regime V_g=-43V (red curve) and at Dirac point V_g=11.2V (green curve) in Fig. VIII-7. The red curve at highly doped regime exhibits two enhanced conductance peaks at V_{bias} =±140μV and a dip around zero bias, while the peaks on the green curve are nearly non-observable.

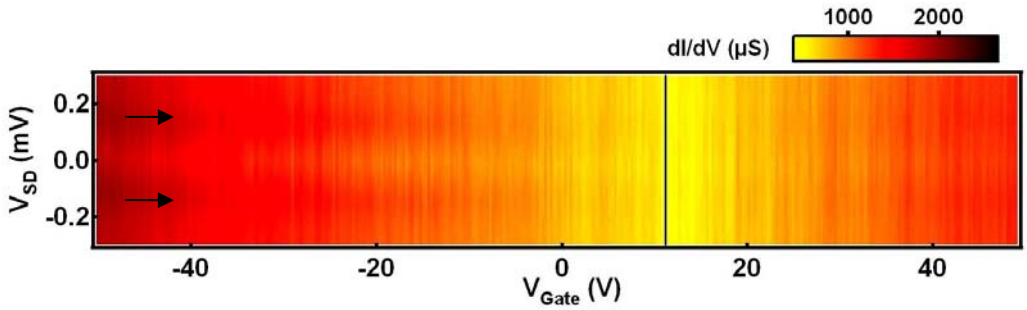

Fig. VIII-6. Differential conductance as a function of bias voltage and back gate voltage, blue line shows the Dirac point of the device, two black arrows point at the conductance peaks at V_{bias} =±140μV.

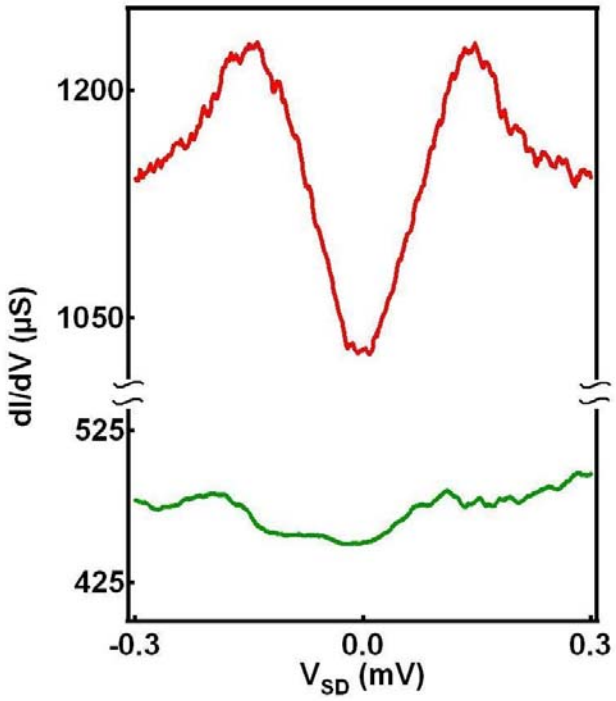

Fig. VIII-7. Differential conductance as a function of bias voltage, red and green curves are at V_g=-43V and 11.2 V respectively.

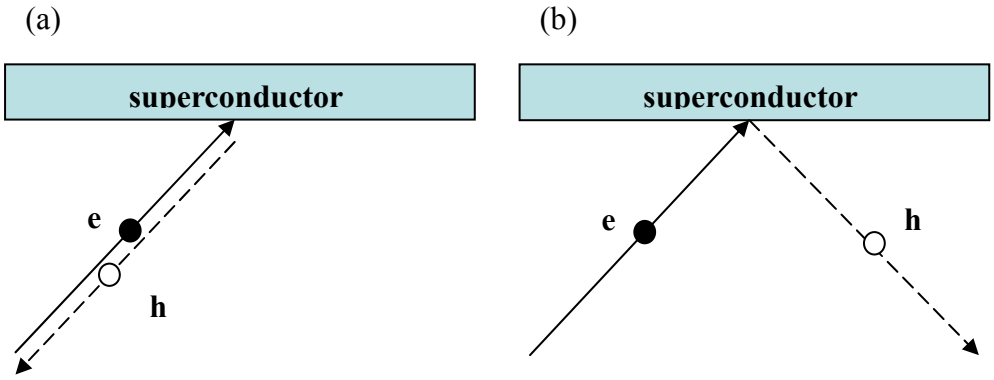

Fig. VIII-8. schematics of electron – hole conversion, (a) retroreflection: reflection angle equals to the incidence angle (b) specular reflection: reflection angle is inverted

The conductance peaks at V_{bias} =±140μV arise from the Andreev reflection. At

the graphene – superconductor interface, the electron is reflected as a hole in two different cases: the path of the reflected hole can either be the same as that of the incident electron (retroreflection), or be its mirror image (specular reflection). Theories predict that the conductance of such a device increases from 4/3 to twice the ballistic value as the bias voltage sweeps from 0 to superconducting energy gap value in the case of retroreflection, and decrease from twice to 4/3 in the case of specular reflection (Beenakker 2006). In Fig. VIII-7, the conductance of the red curve from highly doped conductance starts with dip at the zero bias, and develops to a peak at superconducting energy gap, indicating the Andreev reflection here is mostly retroreflection. As for specular reflection, the electron – hole conversion is predicted to be a conductance-band electron reflected as a valence-band hole (interband), implying that this unusual reflection occurs around Dirac point. However, our data at Dirac point (green curve in Fig. VIII-7) do not show conductance peak around the zero bias voltage. Another critical condition of specular reflection is that Fermi wavelength in the normal region is large compared to the superconducting coherence length. Combining with the ballistic transport case in graphene, we estimate that mobility of graphene around Dirac point should be ~100,000 cm^2 /V s. Our device mobility is far away from the critical value.

The reason that we fail to observe specular reflection is, that our NS device probably is not clean enough, resulting in the non-ballistic transport and low mobility. A potential solution is suspended graphene NS junctions devices. On the suspended

graphene, the mobility is reported as high as 200,000 cm^2/Vs and the transport approaches ballistic. But the wet etching fabrication of suspended graphene with superconducting electrodes could be another challenge, so suspended graphene NS junctions devices made by the shadow mask method (Bao *et al*., 2010) appears to be the most promising route to observation of specular Andreev reflection.

Reference

Akhmerov, A. R., *et al*., Phys. Rev. B 2006, 75, 045426.

Andreev, A.F., *et al*., Sov. Phys. JETP 1964, 19, 1228.

Bao, W., *et al*., Nano Res 2010, 3, 98.

Beenakker, C.W.J., Phys. Rev. Lett. 2006, 97, 067007.

Cheng, S. G., *et al*., Phys. Rev. Lett. 2009, 103.167003.

Du, X., *et al*., Phys. Rev. B 2008, 77, 184507.

Heersche, H.B., *et al*., Nature 2007, 446, 56.

Lutchyn, R.M., *et al*., Phys. Rev. Lett. 2008, 101, 106402.

Miao, F., *et al*., Science 2007, 317, 1530.

Miao, F., *et al*., Solid State Commun. 2009, 149, 1046.

Titov, M., *et al*., Phys. Rev. B 2006, 74,041401 (R).

Chapter VIIII.

Conclusion

Over the past 5 years I have studied two low dimensional carbon systems – CNTs and graphene. We coupled CNTs to superconducting electrodes to form Josephson junctions (JJ), which exhibited Fabry Perot resonance patterns, enhanced differential conductance peaks, multiple Andreev reflection peaks, gate-tunable supercurrent transistor behaviors, hysteretic *I-V* line shape and "superconductor-insulator" transition. The junction behavior can be understood based on the dissipation dynamics and phase diffusion on the model of resistively and capacitively shunted junctions. In addition, we also investigated Fano resonance on a particular device. The transport spectroscopy exhibited "inverse" Coulomb blockade structures superimposed on Fabry Perot resonance patterns, indicating quantum interference between a channel that is well-coupled to the electrodes and another channel that is poorly-coupled channel. Our transport data was reproduced reasonably by the simulation.

For the second system, graphene, we focus on graphene *pnp* junctions. By developing a technique to fabricate suspended top gates, we are able to fabricate exceedingly clean, high quality graphene *pnp* junctions. In the high magnetic fields, we observed quantum hall plateaus at fractional values, which arise from edge state propagation and equilibration in regions with different filling factors, in agreement

with the theoretical predictions. In zero magnetic fields, we observed Fabry Perot conductance oscillations in the bipolar regime, demonstrating the high quality of our devices. For the future work, a number of promising directions, such as charging and localization (Velasco *et al*., 2010), band gap engineering in bilayer graphene *pnp* junctions (Oostinga *et al*., 2008, Ohta, *et al*., 2006, McCann *et al*., 2006, Novoselov *et al*., 2006, Castro *et al*., 2007, Zhang *et al*., 2009, Feldman *et al*., 2009), are being investigated.

As for the graphene NS junctions, we have observed conductance peaks at the superconducting energy gap. However, the intended goal of the project, observation of specular Andreev reflection, was not achieved. This is because specular Andreev reflection mainly takes place when the Fermi level is within the energy gap of the superconductor, thus a very sharp Dirac point is needed. Substrate-supported samples typically have Dirac points broadened to ~ 0.5V in gate voltage, or 20 meV in Fermi Level. Thus an alternate device fabrication method is required. Suspended graphene NS junctions devices could be one of the solutions. As significant progress has been made towards fabrication of high quality suspended devices, we expect that specular Andreev reflection could be observed in the near future.

Reference

Castro, E. V., *et al*., Phys. Rev. Lett. 2007, 99, 216802.

Feldman, B. E., *et al*., Nature Phys. 2009, 5, 889.

McCann, E., *et al*., Phys. Rev. B 2006, 74, 161403.

McCann, E. & Fal'ko, V. I., Phys. Rev. Lett. 2006, 96, 086805.

Novoselov, K. S. *et al*., Nature Phys. 2006, 2, 177.

Ohta, T., *et al*., Science 2006, 313, 951.

Oostinga, J. B., *et al*., Nature Mater. 2008, 7, 151

Velasco Jr., J., *et al*., Phys. Rev. B. 2010, 81, 121407(R).

Zhang, Y. B., *et al*., Nature 2009, 459, 821.

Appendix I.

EBL Parameters

Resist	PMMA	MMA	LOR3B	LOR3A/1A
Thickness (nm)	200	300	300	300/100
Spin speed (r/min)	4000	4000	4000	4000
Spin time (s)	40	40	40	40
Baking temperature (C)	170	170	190	170
Baking time (min)	10	10	5	5
Developer	MIBK		MF319	MF319
Developing time (s)	60~65		5~8	25~30/7~10
Rinse solution	IPA and DI water		DI water	DI water
Rinse time (s)	60 and 60		60	60
Remover	Acetone		PG remover	PG remover
Lift-off time (h)	2		2	2

Table Appendix I-1. EBL parameters.

Appendix II.

Helium3 Fridge Operation Protocol

Appendix II.1 Pre-cooldown Helium bath

1. Pump and flush Helium bath with Nitrogen gas:
    a) Cap the center opening of the main bath.
    b) Connect the main bath exhaust (located next to the port labeled B Heater) to a T-adapter. Connect the 2 ends of the T to a pump and to a hose adapter. Insert a valve and a 0-100mbar gauge either before the hose adapter or before the T.
    c) If the variable temperature insert (VTI) pump is used, make sure the power supply is 3 phase 208 V.
    d) Turn on the pump, wait for several minutes until the pressure in the main bath is <10mBar.
    e) Turn off the pump
    f) Fill it with Nitrogen gas (watch pressure meter, make sure no vacuum inside)
    g) Repeat d-f three steps for a couple of times.
    h) Leave the main bath filled with Nitrogen or Helium gas. Disconnect the pump and put on over-pressure valve.
2. Fill Helium bath with liquid Nitrogen
    a) Insert the stainless steel pipe into Helium port (labeled as such).

b) Connect liquid Nitrogen bottle to the stainless steel pipe with rubber tube.

c) Take off over-pressure-valve.

d) Open liquid Nitrogen valve on the Nitrogen Dewar, control gas flow not too fast not too slow (30 mins~2hours)

e) Close valve when liquid Nitrogen spills out of the main bath exhaust.

Appendix II.2 Prepare the Inner Vacuum Can (IVC)

1. Insert chip carrier into socket. Follow the pin-charts posted on the side of the equipment cabinet.
2. Clean the insert carefully with IPA to remove old vacuum grease
3. Grease both the end of the vacuum end and the insert.
4. Gently guide the vacuum can up to the level of the copper cone seal of the insert. While holding the vacuum can, turn on the pump that pumps IVC, twisting the can in an upward motion to make a good seal.
5. Pump and flush IVC twice with Helium gas

   "T" output IVC port on the top of Helium3 insert

   Connect one of them to VTI pump

   Connect the other one to Helium gas through a valve
6. Put a little (Room Temperature and Pressure) of He gas into IVC as exchange gas.
7. Tape the copper pick-up pipe with Al adhesive tape

Appendix II.3 Transfer liquid Nitrogen to the Nitrogen bath

1. Insert stainless steel pipe into Helium bath, make sure to screw it to the bottom
2. Connect stainless steel pipe to Nitrogen bath with the rubber pipe
3. Pressurize the main bath with Nitrogen gas: connect main bath exhaust to Nitrogen gas, and open Nitrogen gas. Liquid Nitrogen is pressurized to flow from Helium bath to Nitrogen bath.
4. Turn on the Nitrogen level meter so that you can monitor the level.
5. When Helium bath is empty of Liquid Nitrogen (signals: when the level starts to decrease, or when the exhaust suddenly becomes loud), turn off Nitrogen gas.

Appendix II.4 Transfer Liquid Helium to Helium Bath

1. Pump and flush Helium bath again for several times, be sure to read zero on vacuum gauge. If the pressure does not decrease to 1mbar within 10 minutes pumping, there is still liquid Nitrogen inside the bath. DO NOT transfer Helium until all Liquid Nitrogen is removed.
2. Transfer liquid Helium
    a) Open over-pressure-valve
    b) Connect vent port (on liquid Helium Dewar) to Helium gas
    c) Close safety-valve (on liquid Helium Dewar)
    d) The transfer line has two ends. The end with 1 opening facing down should be inserted into the transport dewar. The other end has a screw-on copper

fitting with two slotted holes facing up, and should be inserted into the Helium port. Note: Tighten the copper fitting of the transfer line before transferring.

e) Insert the transfer pipe into the transport dewar slowly. The cold Helium gas will cool down the transfer pipe.

f) If the Helium bath is warm, insert the other side into Helium bath directly. If there is Liquid Helium already present in the bath, wait until liquid Helium comes out of the end. Liquid Helium appears as a short, dense jet of white fog shooting out of the 2 openings at the end of the transfer line, accompanied by large amount of thin, white fog.

g) Push the transfer pipe to the bottom of the transport Dewar bottom, and lift it by 1/2 inch.

h) Open Helium gas to increase pressure in Helium bath

i) Adjust pressure on Helium gas regulator around 5 psi, judging by vapor flow coming out of the main bath. A general rule of thumb: the exhaust should become almost invisible when it rises by about 5 ft.

j) Turn off Helium gas until He bath reaches 80% (lower than Nitrogen level).

Appendix II.5 Lower Helium3 Insert

1. Connect 1K pot to Helium gas

   Turn on Helium gas

Use a beaker of IPA to check Helium gas comes out of pick-up pipe

Tape the pick-up pipe

2. Insert Helium3 insert into fridge slowly, keep Helium gas flowing, through the whole process (this prevents air from getting into the line and forming an ice block)
3. Pump 1K pot by VTI pump, and slightly open needle valve when sorb temperature reaches 4K
4. Pump IVC with VTI pump again if there are too much exchange gas. (The symptom is that the 1K pot temperature does not drop to below 2K when pumping).

Appendix II.6 Running the Magnet

Turn on the power first. Press HOLD

Running the persistent mode:

1. Hold SET POINT and RAISE or LOWER to set the target set point;
2. Press GOTO SET, then wait for current to ramp to the set point;
3. Press HOLD after the set point is reached;
4. Turn HEATER off and **wait for about 5 minutes** (be patient);
5. Press GOTO ZERO and then the persistent mode light will be on.

Getting out of the persistent mode;

1. Check the set point of magnet and see if it's the same as the present magnetic field, which can be checked by pressing "Current Field Status". If not, set it right.

2. Press GOTO SET and wait for current to ramp to the set point,

3. Press HOLD after the set point is reached;

4. Turn HEATER on and **wait for a few minutes** (be patient; going to step 5 too soon may cause the magnet to quench),

5. Now you can change the magnetic field.

Running sweep of magnetic field:

1. Check if the present mode is not persistent mode. If it is, follow step 1-4 of part "changing set point for persistent mode".

2. Hold SET POINT and RAISE or LOWER to set the final set point;

3. Hold SET RATE and RAISE or LOWER to set the sweep rate;

4. Press GOTO SET, then the sweep of magnet field between starting and final set point will start running.

IMPORTANT:

1. Do not turn heater on or off unless the current in the lead (Default Display) matches exactly the current in the magnet (display when pressing "Current Field Status").

2. The maximum magnetic field is 8 T, never set the magnet beyond 8 T

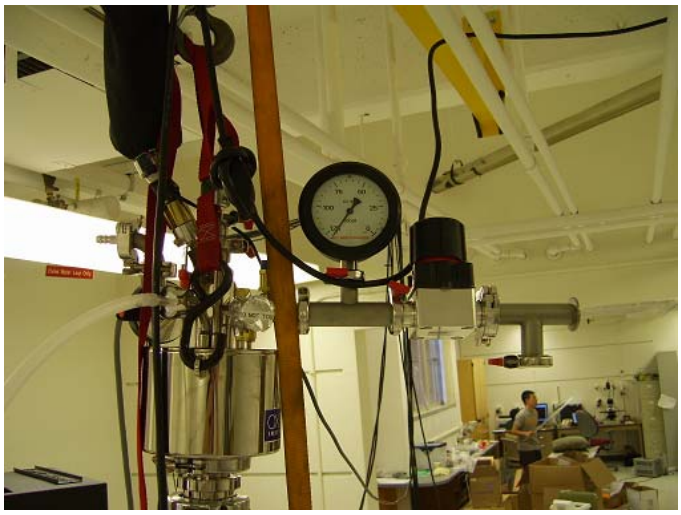

Fig. Appendix II-1. the picture of the top of the Helium3 insert, including 1k port, IVC port and needle valve

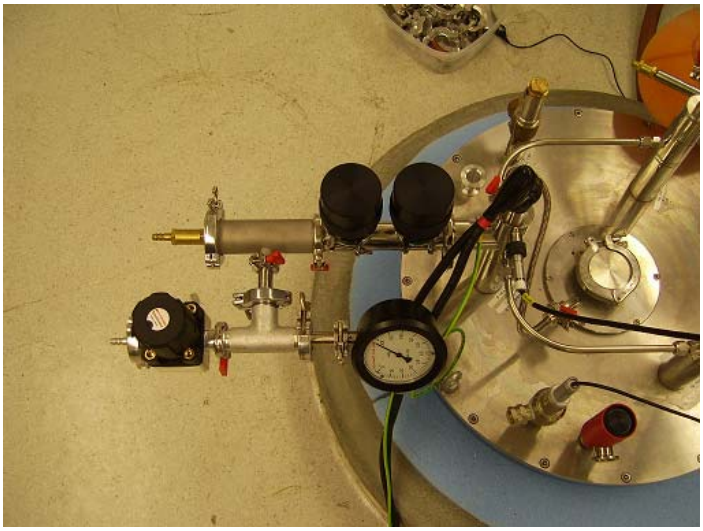

Fig. Appendix II-2. the picture of the fridge.